CFAR Compressed Detection in Heavy-Cluttered Indoor Environments Using IR-UWB Radar: New Experimentally Supported Results

Zaynab Baydoun, Roua Youssef, Emanuel Radoi, Stéphane Azou, Tina Yaacoub

CFAR compressed detection in heavy-cluttered indoor environments using IR-UWB radar: new experimentally supported results

Zaynab Baydoun[(1)], IEEE Student Member, Roua Youssef[(1)], IEEE Member, Emanuel Radoi[(1)], IEEE Senior Member, Stéphane Azou[(2)], IEEE Senior Member, Tina Yaacoub[(3)]

[(1)] Univ Brest, CNRS, UMR 6285 Lab-STICC, F-29200 Brest, France
[(2)] Ecole nationale d'ingénieurs de Brest (ENIB), CNRS, UMR 6285 Lab-STICC, 29280 Plouzané, France
[(3)] Saint Joseph University of Beyrouth, Lebanon

***Abstract*—This paper presents a novel CFAR compressed detection approach for human detection using IR-UWB radar. The associated Xampling scheme operates way below the Nyquist limit and is designed to minimize the sensing matrix coherence, without increasing the implementation complexity. The proposed signal processing architecture aims to detect both moving and stationary people in the framework of heavy-cluttered use cases, such as smart factory indoor environments. In order to address this challenge, we rely on standard radar signal processing, including MTI filtering, noise whitening, and Doppler focusing, but also introduce two new algorithms for joint sparse reconstruction and CFAR detection, in fast-time and range-Doppler domains, respectively. We propose a specific detection statistic, which is proven to be appropriate for both algorithms, its distribution being identified and then validated by standard goodness-of-fit tests. Moreover, it enables reducing the CFAR scheme complexity, since the associated detection threshold is invariant to the noise power, thus making unnecessary its estimation. The proposed approach is finally validated using both simulated and experimentally measured data in an Industry 4.0 indoor environment, for several canonical scenarios. The effectiveness of our CFAR compressed detection algorithms for human detection is thus fully demonstrated, and their performance is assessed and compared to that obtained by signal processing at the Nyquist sampling rate.**

***Index Terms*—UWB, radar detection, compressed sensing, sub-Nyquist sampling, smart factory.**

I. Introduction

Radar systems have played an essential role in various applications, ranging from military and automotive to medical imaging and security. Among these, Impulse Radio Ultra-Wideband (IR-UWB) radar systems have emerged as a significant technological advancement, offering unparalleled capabilities in remote sensing and target detection, especially for short-range and indoor applications [1] [2] [3]. UWB radar systems utilize ultra-short pulses of radio waves transmitted over a broad frequency range, typically spanning several GHz [4]. This unique feature enables UWB radar to provide high-resolution detection and measurement capabilities, making it invaluable in applications where precision is paramount. Moreover, UWB radar can accurately measure not only the distance but also the velocity and other characteristics of objects, making it versatile for various purposes. The multi-functionality of IR-UWB radar is reflected in its widespread adoption across various domains. In military applications, these systems are used for target detection, tracking, and imaging, providing a strategic advantage in complex operational scenarios [5] [6]. In the automotive industry, IR-UWB radar is integrated to advanced driver assistance systems (ADAS) [7] and autonomous vehicles, enhancing safety and enabling features like collision avoidance and parking assistance [8]. IR-UWB radar is utilized in medical imaging for its ability to penetrate materials like clothing and walls, offering non-invasive and high-resolution imaging capabilities [9][10]. Additionally, IR-UWB radar finds applications in industrial settings for level sensing, localization, quality control, and security systems for intrusion detection and surveillance [11].

To ensure the coexistence of IR-UWB systems with other wireless communication technologies, public regulatory bodies have assigned strict constraints for the power spectral density (PSD) of the transmitted UWB signals. It is mainly limited to a maximum level of -41.3 dBm/MHz [12] and constrained by a spectral mask, established by each regulation authority, such as the FCC (Federal Communications Commission) in USA or the ECC (Electronics Communications Committee) in Europe.

While IR-UWB radar systems offer exceptional capabilities, they also come with certain challenges. One of the most important drawbacks is the requirement for a high sampling rate, which leads to the need for complex analog-to-digital converters (ADCs) and high power consumption. This poses significant limitations, especially in battery-powered or resource-constrained applications. An effective solution to address the bottleneck associated with high sampling rates and power consumption is represented by compressed sensing (CS) techniques [13]. They define a groundbreaking signal processing paradigm, which exploits the signal intrinsic sparsity or compressibility in some domains. In the context of IR-UWB radar, CS techniques are able to significantly reduce the number of received signal samples required to capture the essential information, compared to traditional sampling theory. Known as sub-Nyquist sampling or Xampling [14], they lead to more efficient ADCs and lower power consumption. Conversely, CS techniques are also able to recover the information conveyed by the received signal from highly undersampled measurements obtained by Xampling, via sparse reconstruction (SR) algorithms [15].

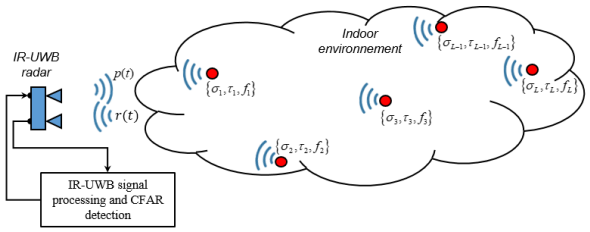

Fig. 1: Indoor environment sensed by an IR-UWB radar

In order to illustrate the suitability of CS techniques for our application, let's consider an indoor environment (Fig. 1), which is seen by the IR-UWB radar as a set of L resolvable scattering points, at the range resolution $\delta R = c/(2B)$, where c and B stand for the speed of electromagnetic waves and the effective band of the T_{rec}-periodically transmitted UWB waveform $p(t)$ respectively. During the q^{th} pulse repetition interval (PRI), the scattering points located at the slant ranges $\{R_l^{(q)}\}_{l=1,\dots,L}$ and having the radial velocities $\{v_l^{(q)}\}_{l=1,\dots,L}$, are characterized by the associated reflectivities $\{\sigma_l^{(q)}\}_{l=1,\dots,L}$, delays $\{\tau_l^{(q)}\} = (2R_l^{(q)})/c\}_{l=1,\dots,L}$ and Doppler shifts $\{f_l^{(q)}\} = (2\nu_l^{(q)})/\lambda_c\}_{l=1,\dots,L}$, with $\lambda_c = c/\nu_c$ and ν_c the central frequency of the UWB pulse spectrum. For the sake of simplicity, note that the upper index (q) is dropped when the signal processing is limited to one PRI or for graphical representations.

The noiseless signal received by the IR-UWB radar during the q-th PRI can be written as:

$$r_q(t) = \sum_{l=1}^{L} \sigma_l^{(q)} p(t - \tau_l^{(q)} - qT_{rec}) e^{j2\pi f_l^{(q)} qT_{rec}}, \quad t \in [qT_{rec}, qT_{rec} + T_r], q = 0, \dots, N_{rec} - 1 \tag{1}$$

where N_{rec} is the number of PRIs and T_r is the fast-time duration of the signal acquisition. Note that T_r is different from the slow-time sampling period T_{rec}, also known as FPS (frames per second) in the case of the Novelda UWB radar introduced below.

As it can be readily seen, since the transmitted UWB waveform $p(t)$ is known to the receiver, $r_q(t)$ is fully characterized by a finite number of parameters $(3L)$ and can therefore be considered as a Finite Rate of Innovation (FRI) signal [16]. Consequently, it admits a minimum sampling rate equal to the number of degrees of freedom per time unit, which is much lower than the Nyquist frequency in the framework of our application. Hence, the CS approach appears to be well suited to IR-UWB radar data acquisition and sparse reconstruction, for human detection in an indoor environment.

Several Xampling schemes have already been proposed [17] [18] for the sub-Nyquist sampling of the IR-UWB signal given in (1). One of these techniques, known as MultiChannel Modulating Waveforms (MCMW) [19], has been chosen for our application because it is proven to be efficient and stable for the compressed sampling of a series of arbitrary pulses. Based on modulation of the received signal with a set of specific random waveforms, followed by an integrator on each parallel signal processing path, this method provides a reduced set of the received signal's Fourier coefficients (FC) $\{c_{k_m}^{(r)}\}_{k_m \in \mathbf{k}_M}$ with $\mathbf{k}_M = \{k_m\}_{m=1,\dots,M}$ the vector of their positions.

Let's denote by $\boldsymbol{y} = [y_1 \quad y_2 \quad \dots \quad y_M]^T$, where $y_m = c_{k_m}^{(r)}$, the measured vector at the output of the Xampling scheme, with $L < M \ll N$ and $N = \lfloor T_r.F_{Nyq} \rfloor$ the number of signal samples during a fast-time acquisition duration, at the Nyquist frequency. Let's also denote by $\mathbf{x}$ the $N \times 1$ sparse vector, which has only L non-zero elements $\{\boldsymbol{x}_{i_l} = \sigma_l e^{j2\pi f_l q T_{rec}}\}_{l=1,\dots,L}$, with $i_l = \lfloor \tau_l.F_{Nyq} \rfloor$. The measured and sparse vectors are related by the following matrix equation:

$$\mathbf{y} = \mathbf{A}\mathbf{x} \tag{2}$$

where $\mathbf{A}$ stands for the $M \times N$ sensing matrix. A detailed description of matrix $\mathbf{A}$ is given in Appendix C.

While the solution of (2) can be found using sparse reconstruction algorithms, its estimation quality strongly depends on the sensing matrix characteristics, which can be equivalently assessed in terms of its spark, Null Space Property (NSP), Restricted Isometry Property (RIP) or coherence [20] [21] [22]. Hence, to improve the sparse reconstruction quality, in this paper we aim at minimizing the sensing matrix coherence (SMC) denoted $\mu_{\mathbf{A}}$, which is given by the highest level of correlation among its columns $\{\mathbf{a}_k\}_{k=1,\dots,N}$:

$$\mu_{\mathbf{A}} = \max_{k \neq l} \left(\frac{|\mathbf{a}_k^H \mathbf{a}_l|}{\|\mathbf{a}_k\|.\|\mathbf{a}_l\|} \right) \tag{3}$$

In a previous work [23], we have addressed the coherence minimization of the sensing matrix with respect to the position vector $\mathbf{k}_M$ of the reduced set of the received signal's FC, in the framework of channel estimation for IR-UWB indoor communications. In another previous work [11], we investigated human detection for collision avoidance using IR-UWB radar in indoor environments. However, the signal acquisition and the proposed subsequent signal processing steps have been performed at the Nyquist sampling frequency. Relying on [23] and [11], we demonstrate in this paper that human detection in a smart factory-like environment can be formulated as a CS problem and we propose an effective solution to solve it. Our main contributions are summarized below:

- We introduce two Orthogonal Matching Pursuit (OMP)-based algorithms for joint sparse reconstruction and CFAR detection, designed to process data recorded during a single and multiple PRIs respectively.
- We propose a correlation-based statistic for CFAR detection, which reduces the CD complexity by making the detection threshold invariant to the noise power.
- We analyze the performance obtained by the CD approach using simulated data. This data is generated based on the CM7 IEEE 802.15.4a channel model utilizing an IR-UWB waveform optimized for maximizing its normalized effective signal power (NESP).
- We demonstrate the effectiveness of the CD approach using measured data, acquired by an IR-UWB radar, in a realistic smart factory-like environment.

- We identify the best trade-off for the $\mathbf{k}_M$ vector selection for both IR-UWB waveforms used in the two scenarios above, in terms of sensing matrix coherence minimization and compressed sampling scheme complexity.

The remainder of the paper is organized as follows. Section II is dedicated to the IR-UWB system model and the formulation of human detection problems in smart factory-like environments, while the proposed approach for signal sparse reconstruction and compressed detection is introduced in Section III. This approach is then validated in Sections IV and V using simulated and measured data respectively. Finally, some conclusions are drawn in Section VI, which also outlines planned future work.

The general notations used in this paper are as follows. Matrices and vectors are denoted by symbols in boldface, including uppercase for matrices and lowercase for vectors. The i^{th} column/row of a matrix $\mathbf{A}$ is denoted by $\mathbf{A}(:,i)$ and $\mathbf{A}(i,:)$ respectively. $(.)^T$, $(.)^H$ and $(.)^\dagger$ represent matrix transpose, Hermitian operator, and Moore-Penrose pseudo-inverse respectively. $\mathbf{I}_M$ denotes the $M \times M$ identity matrix. $\|.\|_k$ and $\|.\|_F$ stand for the l_k-norm and the Frobenius norm, respectively. Some other specific notations are defined in the next sections.

II. System model

While IR-UWB signals have outstanding capabilities in terms of accurate localization, as mentioned in the previous section, their use for human detection in indoor environments remains very challenging, mainly because of the large number of resolvable backscattered signals. Most of these signals are reflections from the scattering points of the indoor environment itself, also known as radar clutter, which prevents the detection of the signals of interest. For smart factory-like indoor environments, the radar clutter can be simulated in a realistic manner using IEEE 802.15.4a channel models [24], which take into account most of the physical large/small-scale characteristics associated with the UWB signal propagation in an industrial indoor environment (delay dispersion, amplitude decay, frequency dependence of the reflectivity ...). More precisely, in this paper, we adopt the CM7 model, associated to line-of-sight (LOS) roomy enclosures like factory halls, filled with a large number of metallic reflectors, robots, plants, etc.

A realization of the IEEE 802.15.4a CM7 environment impulse response is shown in Fig. 2. Note that the radar reception is enabled only for ranges larger than 0.8 m, to avoid direct reception of the transmitted pulse. As it can be readily noticed, this impulse response corresponds to a heavily cluttered environment, which is likely to make human detection very challenging. Moreover, with more than 450 backscattered signals having significant amplitudes (90 % of the cumulated energy), it results in an innovation rate of $3L/T_r$ (about 20×10^9), which roughly corresponds to a sampling frequency equivalent to the Nyquist limit, thus making compressed sensing irrelevant and useless in this context.

Nevertheless, it can also be noticed that for such an indoor environment, most scattering points are fixed, resulting in null

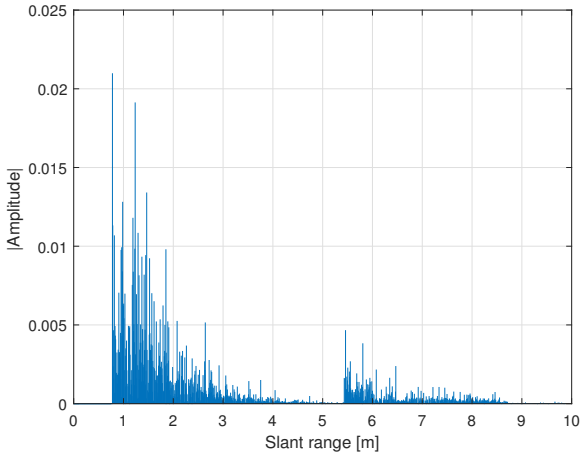

Fig. 2: Impulse response of a LOS industrial indoor environment simulated according to IEEE 802.15.4a CM7 model

Doppler shifts associated to the clutter signals, excepting those backscattered by mobile robots or plant components. On the other hand, the signals of interest for human detection can be characterized by a specific Doppler signature, resulting from people's motion and breathing. Consequently, it is possible to remove most radar clutter by using a moving target indicator (MTI) filter [25], thus making human detection tractable within the compressed sensing framework. Note that the MTI filtering can be performed either in the RF domain, using delay lines complying with the signal frequency characteristics, or after the analog-to-digital conversion, using digital filters. A simple yet effective 1^{st} order MTI filter consists in subtracting the signals corresponding to each couple of consecutive PRI:

$$
\begin{aligned}
& r_q^{(MTI)}(t) = r_q(t) - r_{q-1}(t - T_{rec}) \\
& = \sum_{l=1}^{L} \sigma_l^{(q)} p(t - \tau_l^{(q)} - qT_{rec}) e^{j2\pi f_l^{(q)} qT_{rec}} \\
& \quad - \sum_{l=1}^{L} \sigma_l^{(q-1)} p(t - \tau_l^{(q-1)} - qT_{rec}) e^{j2\pi f_l^{(q-1)} (q-1)T_{rec}} \\
& \Rightarrow r_q^{(MTI)}(t) = \sum_{l=1}^{L} \Big(\sigma_l^{(q)} p(t - \tau_l^{(q)} - qT_{rec}) e^{j2\pi f_l^{(q)} qT_{rec}} \\
& \quad - \sigma_l^{(q-1)} p(t - \tau_l^{(q-1)} - qT_{rec}) e^{j2\pi f_l^{(q-1)} (q-1)T_{rec}} \Big)
\end{aligned}
\tag{4}
$$

Thus, according to (4) the signals backscattered by fixed objects from the indoor environment are completely canceled in the ideal case because the corresponding delays and reflectivities do not vary from a PRI to another, while the associated Doppler shifts are null.

When the signal is sampled at the Nyquist frequency, the system block diagram is shown in Fig. 3. While the processing flow includes some well-known stages, such as MTI, noise whitening, matched filtering (MF), and Doppler focusing (DF), there are also some significant differences compared to the standard radar processing, which justify this

particular system structure. The most important is that in a standard narrowband radar system, the targets remain in the same range resolution cells during the coherent integration time T_{coh} associated with DF, when typical values of the target velocity, pulse repetition frequency (PRF), and range resolution are considered. However, this is not the case in our application, especially due to the signal's huge bandwidth, which results in a very fine range resolution, typically of about 10 cm. Obviously, the CFAR detection is also still carried out after DF to identify standing people using the Doppler frequency associated to their breathing (~ 0.4 Hz). Moreover, the Doppler patterns corresponding to walking people can be further analyzed in order to discriminate them from other artificial moving targets. Finally, position filtering and people tracking can be also implemented when data from several UWB radars are available. However, note that only human detection is addressed in the following, the other tasks, represented in dashed line in Fig. 3, being outside the scope of this paper.

In the case of compressed detection, the proposed system block diagram is shown in Fig. 4. MCMW is first applied to obtain a reduced set of the received signal's FC. The sampling frequency associated to this Xampling scheme is the same as the signal PRF and is much lower than the Nyquist sampling frequency used by the ADC in Fig. 3. The resulting FC are then processed by the MTI filter implemented in digital domain, as already stated in the previous section.

The sparse reconstruction of the signals of interest can be performed with the OMP technique [26][27][28], which is a widely used greedy algorithm. Indeed, OMP provides the delays and the amplitudes corresponding to the echoes from the targets of interest, which is equivalent to estimating the signals of interest when the transmitted IR-UWB waveform is known. Nevertheless, in its original form, OMP algorithm does not enable the control of the false alarm rate. Two versions of this algorithm, which undertake the CFAR detection task in fast-time (single snapshot) and after Doppler focusing (multiple snapshots), are then proposed in the next section. The two proposed algorithms are denoted by CFAR-UWB-OMP and CFAR-UWB-MSOMP, respectively in Fig. 4.

III. Signal sparse reconstruction and compressed detection

The sparse solution of the equation (2), provided by a greedy reconstruction algorithm, is obtained by solving the following constrained optimization problem:

$$\hat{\mathbf{x}} = \underset{\mathbf{x}}{\operatorname{argmin}} \|\mathbf{y} - \mathbf{A}\mathbf{x}\|_2^2, \text{ subject to } \|\mathbf{x}\|_0 \leq L \tag{5}$$

It can be demonstrated [29] that the OMP algorithm provides a unique solution corresponding to the global optimum provided that:

$$\begin{cases} L < (1 + 1/\mu_{\boldsymbol{A}})/2 \\ M \geq 2L\ln(N) \end{cases} \tag{6}$$

Actually, these conditions are very restrictive in the framework of CFAR detection [30]. Indeed, OMP algorithm still provides good performance in terms of detection rate, even if they are not strictly met, provided that the values of L and M are not too far from the theoretical limits above. Thus, a particular attention should be especially paid to the sensing matrix coherence $\mu_{\boldsymbol{A}}$, since the lower its value, the better the OMP's reconstruction performance.

The design of low coherence sensing matrices has already been extensively addressed and important theoretical results have been obtained. Thus, when no prior constraints are defined for the sensing matrix, it was demonstrated that random Gaussian matrices are able to satisfy RIP with high probability and to provide the lowest coherence levels for the sensing matrix [31] [32]. However, they are not suitable for our application, since the structure of the sensing matrix is constrained by the selected MCMW Xampling scheme and is expressed as follows [33]:

$$\mathbf{A} = \mathbf{\Phi}\mathbf{\Psi} \tag{7}$$

with $\mathbf{\Phi}$ the diagonal $M \times M$ matrix of the transmitted waveform's FC $\{c_{k_m}^{(p)}\}_{k_m \in \mathbf{k_M}}$, and $\mathbf{\Psi}$ the $M \times N_{DFT}$ reduced DFT matrix $\{e^{-j2\pi k_m n/N_{DFT}}\}_{k_m \in \mathbf{k_M}, n=0,\ldots,N_{DFT}-1}$ as explained in Appendix C.

We demonstrated in [23] that the coherence of this particular sensing matrix is given by the equation below, where $\beta_{k_m} = |c_{k_m}^{(p)}|^2$ and $\mathbf{\Sigma}_{\mathbf{k}_M}(n) = \{\cos(\frac{2\pi n(k_l - k_m)}{N})\}$, with $k_m \in \mathbf{k_M}, k_l \in \mathbf{k_M}$:

$$\mu_{\mathbf{A}}(\mathbf{k}_M) = \max_{n=1,\ldots,N-1} \sqrt{\frac{\boldsymbol{\beta}_{\mathbf{k}_M}^T \mathbf{\Sigma}_{\mathbf{k}_M}(n) \boldsymbol{\beta}_{\mathbf{k}_M}}{\boldsymbol{\beta}_{\mathbf{k}_M}^T \mathbf{1}_M \boldsymbol{\beta}_{\mathbf{k}_M}}} \tag{8}$$

According to this equation, the sensing matrix coherence depends only on the selected set of transmitted waveform's FC $\left\{c_{k_m}^{(p)}\right\}_{k_m \in \mathbf{k}_M}$. Selecting consecutive coefficients makes the MCMW scheme design simpler, but results in high values of $\mu_{\mathbf{A}}$. On the other hand, a fully random selection of the FC is likely to provide the lowest coherence values, but is very challenging for the MCMW scheme implementation, since it requires very selective filters. A good trade-off between the MCMW hardware complexity and the sparse reconstruction accuracy can be found by combining these two opposite approaches for selecting the transmitted waveform's FC. Hence, in this paper, we adopt the same strategy as in [14], which consists of selecting 4 groups of 4 consecutive FC, whose positions inside the UWB signal bandwidth are chosen to minimize the sensing matrix coherence.

The FC corresponding to the same positions $\mathbf{y} = \left\{c_{k_m}^{(r)}\right\}_{k_m \in \mathbf{k}_M}$ are obtained at the output of the Xampling scheme, using 4 MCMW 4-channels schemes. If $\mathbf{w} = \left\{c_{k_m}^{(w)}\right\}_{k_m \in \mathbf{k}_M}$ denotes the FC vector associated with the clutter and noise, the input vector for the CS processing flow can be expressed as:

$$\mathbf{y} = \mathbf{A}\mathbf{x} + \mathbf{w} \tag{9}$$

It is worth noting that no sparse reconstruction method can be used to solve (9), simply because the solution vector $\mathbf{x}$ is not sparse at this stage. Indeed, as shown in the previous section, the clutter associated with the CM7 indoor environment is very

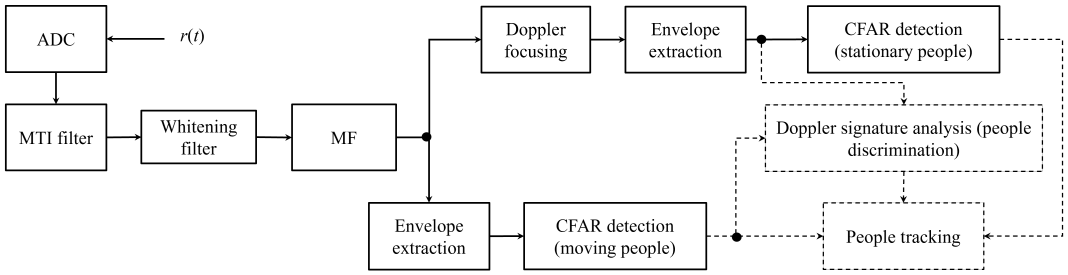

Fig. 3: Block diagram of Nyquist signal processing

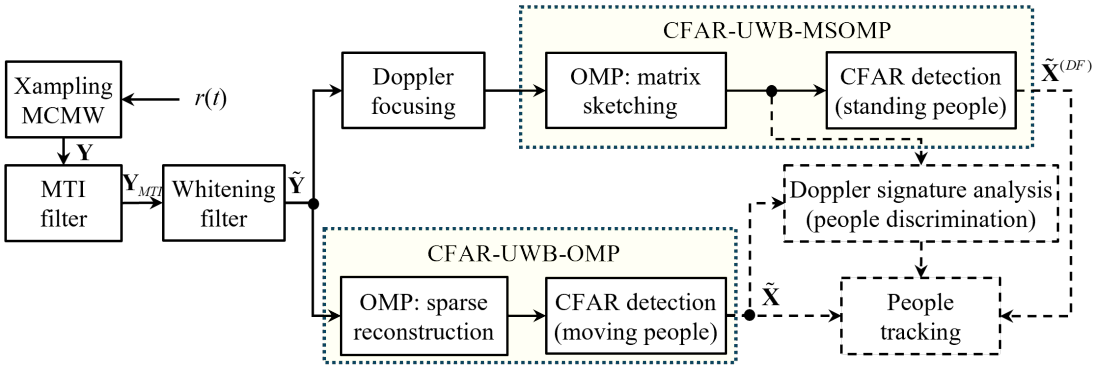

Fig. 4: Block diagram for people compressed detection in an indoor environment

rich in multipaths, which results in a high number of non-zero components of the solution vector $\mathbf{x}$, thus making their accurate estimation using sparse reconstruction algorithms like OMP intractable. The MTI filtering is an effective way to solve this problem, as already discussed in the previous section. In the framework of our application, we have used a 1^{st} order digital filter with the transfer function: $H_{MTI}(z) = 1 - z^{-1}$.

However, although this processing step can remove most of the clutter, it also introduces a strong attenuation in the low-frequency domain. The consequence is that the Doppler shifts associated with human breathing, typically below 1 Hz, become more difficult to detect. A whitening filter (WHT) can then be included to compensate for the effect of MTI filtering in the low-frequency domain and improve the detection of stationary people after the Doppler focusing stage. The WHT filter used in our application is a standard 1^{st} order autoregressive (AR) filter having the transfer function: $H_{WHT}(z) = \frac{1}{1-az^{-1}}$, with $a = 0.99$, which is considered the maximum value of this coefficient that still meets the filter's stability requirement in practical implementations. It can be readily checked that the WHT filter enables an overall attenuation of the signal backscattered by a breathing person of only 2.1 dB, compared with 44 dB at the MTI filter output.

A. Single snapshot algorithm

Let us consider now the matrix $\mathbf{Y}$ obtained by concatenating the column vectors $\{\mathbf{y}_q\}_{q=1,\ldots,N_{rec}}$ measured during N_{rec} successive PRI and denote by $\mathbf{X}$ and $\mathbf{W}$ the $N \times N_{rec}$ matrices whose columns are the corresponding solution vectors $\{\mathbf{x}_q\}_{q=1,\ldots,N_{rec}}$ and clutter and noise vectors $\{\mathbf{w}_q\}_{q=1,\ldots,N_{rec}}$. The equation (9) takes the following matrix form in this case:

$$\mathbf{Y} = \mathbf{A}\mathbf{X} + \mathbf{W} \tag{10}$$

Finally, if we denote by $\mathbf{C}_{MTI}$ and $\mathbf{C}_{WHT}$ the convolution matrices corresponding to the MTI and whitening filters, respectively, (10) can be rewritten in the form:

$$\tilde{\mathbf{Y}} = \mathbf{A}\tilde{\mathbf{X}} + \tilde{\mathbf{W}} \tag{11}$$

where $\tilde{\mathbf{Y}} = \mathbf{Y}\mathbf{C}_{MTI}\mathbf{C}_{WHT}$, $\tilde{\mathbf{X}} = \mathbf{X}\mathbf{C}_{MTI}\mathbf{C}_{WHT}$, and $\tilde{\mathbf{W}} = \mathbf{W}\mathbf{C}_{MTI}\mathbf{C}_{WHT}$.

Each column of the $\tilde{\mathbf{X}}$ matrix is now sparse and can be recovered using the OMP algorithm, for subsequent CFAR detection. However, as already stated in the previous section, in its original form, OMP is not suitable for dealing with this problem. Hence, we propose a modified version, called CFAR-UWB-OMP taking into account the UWB waveform characteristics and performing an effective CFAR detection. Indeed, a standard cell-averaging CFAR (CA-CFAR) technique [34] relies on a noise amplitude-based detection statistic. The associated detection threshold must be constantly updated, since it depends on the noise mean power, which is likely to vary over time. Instead, we propose to use the maximum normalized correlation coefficient between the residual and the columns of the sensing matrix, denoted by $c_{max}^{(corr)}$, as detection statistic. In this case, the detection threshold is invariant to the noise power and depends only on the UWB waveform shape and sensing matrix coherence, as will be shown in Section IV.

Algorithm 1 below summarizes the processing flow associated with the joint sparse reconstruction and CFAR detection in fast-time (one snapshot). It operates on each column of the

data matrix $\tilde{\mathbf{Y}}$ at the output of the whitening filter, which is denoted by $\tilde{\mathbf{y}}$ and corresponds to the current PRI.

Algorithm 1 CFAR-UWB-OMP

Input: The $M \times 1$ data vector $\tilde{\mathbf{y}}$ at the output of the whitening filter, the $M \times N$ sensing matrix $\mathbf{A}$, the detection threshold Th_{det} and the maximum number of expected targets during a PRI N_{tg}.
Initialization:
$\tilde{\mathbf{x}}_0 = \mathbf{0}_{N\times 1}$: the reconstructed sparse vector (solution vector).
$\mathbf{r}_0 = \tilde{\mathbf{y}}$: the residual vector.
$\theta_0 = [\|\mathbf{r}_0\|]$: the vector of residual vector norms.
$\mathbf{i}_0 = [\,]$: the vector of non-zero component positions of the solution vector.
$\mathbf{c}_0^{corr} = [\,]$: the vector of correlation coefficients corresponding to the non-zero components of the solution vector.
$\underline{\tilde{\mathbf{x}}}_0 = [\,]$: the vector containing only the non-zero components of the solution vector.
$n = 0$ and $f_{stop} = 0$: index and stop flag used inside the *while* loop.
while $n \leq N_{tg}$ and $f_{stop} = 0$ **do**
  Find the column of the matrix $\mathbf{A}$ the most correlated with the residual $\mathbf{r}_n$: $i_{max}^{(n)} = \underset{\substack{i\notin \mathbf{i}_n \\ i=1,\ldots,N}}{\operatorname{argmax}} \frac{|\mathbf{r}_n^H \mathbf{a}_i|}{\|\mathbf{r}_n\|.\|\mathbf{a}_i\|}$
  if $c_{max}^{(corr)} = \frac{|\mathbf{r}_n^H \mathbf{a}_{i_{max}^{(n)}}|}{\|\mathbf{r}_n\|\|\mathbf{a}_{i_{max}^{(n)}}\|} \leq Th_{det}$ **then**
    $f_{stop} = 1$
  else
    $n \leftarrow n+1$ and :
    Update $\mathbf{i}_n = [\mathbf{i}_{n-1} \quad i_{max}^{(n-1)}]$
    And $\mathbf{c}_n^{(corr)} = [\mathbf{c}_{n-1}^{(corr)} \quad c_{max}^{(corr)}]$, $\underline{\mathbf{A}}_n = \mathbf{A}(:, \mathbf{i}_n)$
    $\underline{\tilde{\mathbf{x}}}_n = \underline{\mathbf{A}}_n^{\dagger}\tilde{\mathbf{y}}, \mathbf{r}_n = \tilde{\mathbf{y}} - \underline{\mathbf{A}}_n^H \underline{\tilde{\mathbf{x}}}_n$
    Update $\theta_n = [\theta_{n-1} \quad \|\mathbf{r}_n\|]$
  end if
end while
Set the $N \times 1$ solution vector: $\tilde{\mathbf{x}} = \mathbf{0}_{N\times 1}$, $\tilde{\mathbf{x}}(\mathbf{i}_n) = \underline{\tilde{\mathbf{x}}}_n$
Output: The sparse vector solution $\tilde{\mathbf{x}}$, the vector of non-zero component positions of the solution vector $\mathbf{i}_n$, the vector of correlation coefficients corresponding to the non-zero components of the solution vector $\mathbf{c}_n^{(corr)}$ and the vector of residual norms θ_n.

Compared to the standard OMP, the proposed algorithm introduces a detection threshold Th_{det}, which is defined to ensure the required false alarm probability (P_{fa}) level. Thus, the iterations are stopped and new non-zero components for the solution vector are no longer extracted as soon as $c_{max}^{(corr)} < Th_{det}$.

The detection threshold is calculated using a $M \times N_{noise}$ sample matrix $\tilde{\mathbf{W}}_{sample}$ of residual clutter plus noise at the output of the whitening filter. Thus, the same algorithm is first used with $Th_{det} = 0$ to extract the $N_{tg} \times N_{noise}$ correlation coefficients $c_{max}^{(corr)}$ from this data (N_{tg} correlation coefficients for each PRI).

The statistical analysis we have carried out in order to identify the distribution providing the best fit for these correlation coefficients revealed that they are well matched by the generalized extreme value (GEV) law [35], as shown in Fig. 5(a). Our finding is not surprising since, according to the extreme value theorem, the GEV distribution is the only possible limit distribution of properly normalized maxima of a sequence of independent and identically distributed random variables [36]. This hypothesis has been further validated by simulation, by comparing the required and estimated false alarm rates, and using both the chi-square and Kolmogorov-Smirnov Goodness-of-Fit (GoF) tests, with a significance level $\alpha = 0.01$, which is the probability of rejecting the true distribution.

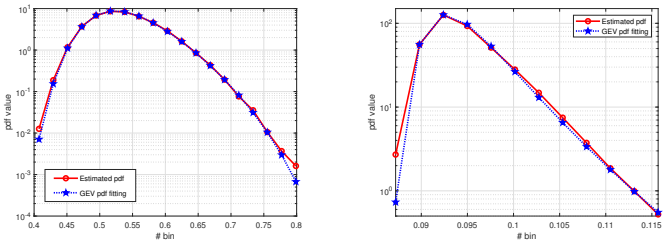

(a) (b)

Fig. 5: Estimated pdf fitting for the correlation coefficients associated to the non-zero components extracted with: (a) CFAR-UWB-OMP (b), CFAR-UWB-MSOMP

Consequently, we next estimate the GEV distribution parameters (location parameter $\lambda \in \mathbb{R}$, scale parameter $\sigma > 0$, and shape parameter $\xi \in \mathbb{R}$) providing the best goodness-of-fit for the correlation coefficients extracted from the data in $\tilde{\mathbf{W}}_{sample}$. Finally, we calculate the detection threshold for CFAR-UWB-OMP corresponding to the required P_{fa} using the inverse cumulative GEV distribution [37]:

$$Th_{det} = F^{-1}_{\hat{\lambda},\hat{\sigma},\hat{\xi}}(1-P_{fa}) = \begin{cases} \hat{\lambda} - \frac{\hat{\sigma}}{\hat{\xi}}\left[1-(-\ln(1-P_{fa}))^{-\hat{\xi}}\right], & \hat{\xi} \neq 0 \\ \hat{\lambda} - \hat{\sigma}\ln(-\ln(1-P_{fa})), & \hat{\xi} = 0 \end{cases} \quad (12)$$

where $(\hat{\lambda}, \hat{\sigma}, \hat{\xi})$ are the data-based estimated parameters of the best-fitted GEV distribution.

The CFAR-UWB-OMP algorithm is well suited to detect moving targets, which continuously change the range resolution cell. The DF is not effective in this case because it requires that a detected target remains in the same resolution cell during the coherent integration time. Nevertheless, the DF is a much better solution for detecting stationary people. Indeed, although they are not moving, their backscattering signal is not removed by the MTI filter because of the Doppler shift associated to the human breathing. Since the breathing rate is almost constant for a standing person, it can be detected using the DF technique.

As for the Nyquist signal processing, the DF is performed by taking the Fourier transform of the signal in each range resolution cell (slow-time processing), but at the output of the whitening filter rather than at the output of the MF. In the following subsection, we will establish the signal model for the DF focusing in the CS processing framework.

B. Multiple snapshots algorithm

Let us consider again the matrix equation (11), which lies in the fast-time (range) vs slow-time domain. The matrix $\hat{\mathbf{X}}$ contains one non-zero value in each column for each target, located in a position given by its range from the radar during the current PRI. Obviously, for a stationary target with a non-null Doppler shift there will be as many non-zero values as columns, on the row corresponding to its range from the radar. However, all these values reduce to only one in the range-Doppler domain, after taking the data row-wise Fourier transform:

$$\tilde{\mathbf{X}}^{(\mathbf{DF})} = \tilde{\mathbf{X}}\mathbf{F}_{N_{rec}} \Rightarrow \tilde{\mathbf{X}} = \tilde{\mathbf{X}}^{(\mathbf{DF})}\mathbf{F}_{N_{rec}}^{H} \tag{13}$$

where $\mathbf{F}_{N_{rec}}$ is the $N_{rec} \times N_{rec}$ Discrete Fourier Transform (DFT) matrix.

Consequently, the $\tilde{\mathbf{X}}^{(DF)}$ matrix has a sparsity level much higher than $\tilde{\mathbf{X}}$ for this type of targets. In this case, (11) can be rewritten in the following form:

$$\begin{aligned} \tilde{\mathbf{Y}} &= \mathbf{A}\tilde{\mathbf{X}} + \tilde{\mathbf{W}} \Rightarrow \tilde{\mathbf{Y}} = \mathbf{A}\tilde{\mathbf{X}}^{(DF)}\mathbf{F}_{N_{rec}}^{H} + \tilde{\mathbf{W}} \\ &\Rightarrow \tilde{\mathbf{Y}}\mathbf{F}_{N_{rec}} = \mathbf{A}\tilde{\mathbf{X}}^{(DF)}\mathbf{F}_{N_{rec}}^{H}\mathbf{F}_{N_{rec}} + \tilde{\mathbf{W}}\mathbf{F}_{N_{rec}} \\ &\Rightarrow \check{\mathbf{Y}} = \mathbf{A}\tilde{\mathbf{X}}^{(DF)}\mathbf{B}^{H} + \check{\mathbf{W}} \end{aligned} \tag{14}$$

where $\mathbf{B}^{H} = \mathbf{F}_{N_{rec}}^{H}\mathbf{F}_{N_{rec}} = \mathbf{I}_{N_{rec}}$ while $\check{\mathbf{Y}} = \tilde{\mathbf{Y}}\mathbf{F}_{N_{rec}}$ and $\check{\mathbf{W}} = \tilde{\mathbf{W}}\mathbf{F}_{N_{rec}}$ are the signal and noise matrices respectively, after the Doppler focusing.

Note that the problem of recovering the sparse solution of (14) is equivalent to the previous problem in (11), for an equivalent $MN_{rec} \times NN_{rec}$ sensing matrix $\mathbf{A}_{ech} = \mathbf{A} \otimes \mathbf{B}$, where $\otimes$ stands for the Kronecker product. As it is demonstrated in Appendix B, the coherence of both matrices $\mathbf{A}$ and $\mathbf{A}_{ech}$ is the same when $\mathbf{B} = \mathbf{I}_{N_{rec}}$. Hence, if the matrix $\mathbf{A}$ is optimized for the sparse reconstruction problem in (11), it will be also optimized for the second one in (14).

The solution of (14) can be found using the OMP matrix sketching algorithm [38]. Actually, we propose a modified version, called CFAR-UWB-MSOMP and described by Algorithm 2, which also enables the control of the false alarm rate. Note that unlike the Algorithm 3 given in [38], our algorithm is able to work with complex vectors/matrices and allows solution matrices $\tilde{\mathbf{X}}^{(DF)}$ of arbitrary size $N \times N_{rec}$, not limited to being square.

Just as for the Algorithm 1 introduced above, the same GEV distribution, but with different parameters, has been identified, by statistical analysis and using the same GoF tests, as providing the best fit for the correlation coefficients (see Fig. 5(b). Consequently, the detection threshold is provided by the same equation (12), using the GEV distribution's shape, scale, and location parameters estimated from a $M \times N_{noise}$ sample matrix $\check{\mathbf{W}}_{sample}$ of residual clutter plus noise at the DF output.

It is worth noting that, unlike the previously discussed one snapshot sparse reconstruction, in this case the objective is to find the couple of indices $[i_{max}^{(n)}\, l_{max}^{(n)}]$ of the current extracted component, instead of the single index $i_{max}^{(n)}$. In [38], they are determined using the following relationship:

$$[i_{max}^{(n)}\, l_{max}^{(n)}] = \underset{[i\, l] \notin \mathbf{\Lambda}_n}{\operatorname{argmax}} |\mathbf{a}_i^H \mathbf{R}_n \mathbf{b}_l| \tag{15}$$

Algorithm 2 CFAR-UWB-MSOMP

Input: The $M \times N_{rec}$ data matrix $\check{\mathbf{Y}}$ at the output of the DF, the $M \times N$ and $N_{rec} \times N_{rec}$ sensing matrix $\mathbf{A}$ and $\mathbf{B}$ respectively, the detection threshold Th_{det} and the maximum number of expected targets in the range-Doppler domain N_{tg}.
Initialization:
$\tilde{\mathbf{X}}_0^{(DF)} = \mathbf{0}_{N \times N_{rec}}$: the reconstructed sparse matrix (solution matrix).
$\mathbf{R}_0 = \check{\mathbf{Y}}$: the residual matrix.
$\theta_0 = [\|\mathbf{R}_0\|_F]$: the vector of residual matrix Frobenius norm.
$\varepsilon \ll 1$: positive constant used to stop the algorithm when the residual matrix norm becomes too small.
$\mathbf{\Lambda}_0 = [\,]$: the 2-columns matrix containing the indices of the solution matrix non-zero components.
$\mathbf{c}_0^{corr} = [\,]$: the vector of correlation coefficients corresponding to the non-zero components of the solution vector.
$\check{\mathbf{x}}_0 = [\,]$: the vector containing the amplitudes of the solution matrix only for its non-zero components.
$a_{max} = \max_{i=1,\ldots,N} \|\mathbf{a}_i\|$, $b_{max} = \max_{l=1,\ldots,N_{rec}} \|\mathbf{b}_l\|$
$n = 0$ and $f_{stop} = 0$: index and stop flag used inside the **while** loop.
while $n \leq N_{tg}$ and $f_{stop} = 0$ **do**
  Find the indices of the current non-zero component of the solution matrix $\tilde{\mathbf{X}}^{(DF)}$ by solving the maximization problem: $[i_{max}^{(n)}\ l_{max}^{(n)}] = \operatorname{argmax}_{[i\ l] \notin \mathbf{\Lambda}_n} |\mathbf{a}_i^H \mathbf{R}_n \mathbf{b}_l|$
  if $c_{max}^{(corr)} = \frac{\left|\mathbf{a}_{i_{max}^{(n)}}^H \mathbf{R}_n \mathbf{b}_{l_{max}^{(n)}}\right|}{a_{max} b_{max} s_{max}^{(n)}} < Th_{det}$ **then**
    $f_{stop} = 1$
  else
    $n \leftarrow n + 1$ and:
    Update $\mathbf{\Lambda_n} = \begin{bmatrix} \mathbf{\Lambda}_{n-1} \\ i_{max}^{(n-1)} \quad l_{max}^{(n-1)} \end{bmatrix}$
    And $\mathbf{c}_n^{(corr)} = [\mathbf{c}_{n-1}^{(corr)} \quad c_{max}^{(corr)}]$
    Compute the $n \times n$ matrix $\mathbf{D}^{(n)}$, with $d_{r,q}^{(n)} = \mathbf{b}_{\mathbf{\Lambda}_n(q,2)}^H \mathbf{b}_{\mathbf{\Lambda}_n(r,2)} \mathbf{a}_{\mathbf{\Lambda}_n(r,1)}^H \mathbf{a}_{\mathbf{\Lambda}_n(q,1)}$, and the $n \times 1$ vector $\mathbf{d}^{(n)} = [\mathbf{a}_{\mathbf{\Lambda}_n(1,1)}^H \check{\mathbf{Y}} \mathbf{b}_{\mathbf{\Lambda}_n(1,2)} \ldots \mathbf{a}_{\mathbf{\Lambda}_n(n,1)}^H \check{\mathbf{Y}} \mathbf{b}_{\mathbf{\Lambda}_n(n,2)}]^T$
    Solve $\check{\boldsymbol{x}}_n = (\mathbf{D}^{(n)})^{-1} \mathbf{d}^{(n)}$
    Find the new residual matrix $\mathbf{R}_n = \check{\mathbf{Y}} - \mathbf{A}\tilde{\mathbf{X}}_n^{(DF)}\mathbf{B}^T$, where $\tilde{\mathbf{X}}_n^{(DF)} = \sum_{i=1}^{n} \check{\mathbf{x}}_n(i) \mathbf{a}_{\mathbf{\Lambda}_n(i,1)} \mathbf{b}_{\mathbf{\Lambda}_n(i,2)}^H$
    Calculate the maximum singular value of $\mathbf{R}_n$: $s_{max}^{(n)} = \|\mathbf{R}_n\|_F$, and add it to the vector of the residual matrix Frobenius norm $\theta = [\theta_{n-1} \quad s_{max}^{(n)}]$.
    if $s_{max}^{(n)} < \epsilon \|\mathbf{R}_0\|_F$ **then**
      $f_{stop} = 1$
    end if
  end if
end while
Set the $N \times N_{rec}$ solution matrix: $\tilde{\mathbf{X}}^{(DF)} = \mathbf{0}_{N \times N_{rec}}, \tilde{\mathbf{X}}^{(DF)}(\mathbf{\Lambda}_n(i,1), \mathbf{\Lambda}_n(i,2)) = \check{\mathbf{x}}_n(i), i = 1 \ldots n$
Output: The sparse matrix solution $\tilde{\mathbf{X}}^{(DF)}$, the matrix $\mathbf{\Lambda}_n$ of non-zero component indices of the solution matrix, the vector of correlation coefficients $\mathbf{c}_n^{(corr)}$ corresponding to the non-zero components of the solution matrix, and the vector of residual matrix norm θ_n.

where $\mathbf{\Lambda}_n$ is the 2-columns matrix whose n^{th} row $[\lambda_n(1)\ \lambda_n(2)] = [i_{max}^{(n)}\ l_{max}^{(n)}]$ contains the indices of $\tilde{\mathbf{X}}^{(DF)}$ matrix non-zero component extracted at the n^{th} iteration and $\mathbf{R}_{n-1} = \tilde{\mathbf{Y}} - \mathbf{A}\tilde{\mathbf{X}}_{n-1}^{(DF)}\mathbf{B}^H$ is the residual matrix at the $(n-1)^{th}$ iteration.

Nevertheless, since our algorithm not only extracts the $\tilde{\mathbf{X}}^{(DF)}$ non-zero components but also performs the CFAR detection, the maximized value in (15) has to be normalized, in order to remove the dependence of the detection threshold on the noise power. Relying on the inequality below:

$$|\mathbf{a}_i^H \mathbf{R}_n \mathbf{b}_l| \leq a_{max} b_{max} s_{max}^{(n)} \tag{16}$$

where $s_{max}^{(n)} = \|\mathbf{R}_n\|_F$ is the maximum singular value of $\mathbf{R}_n$, $a_{max} = \max_{i=1,\dots,N} \|\mathbf{a}_i\|$ and $b_{max} = \max_{i=1,\dots,N_{rec}} \|\mathbf{b}_l\|$, we define the following normalized correlation coefficient, which will be further used in Algorithm 2 as decision statistic:

$$c_{i,l}^{(corr)}(n) = \frac{|\mathbf{a}_i^H \mathbf{R}_n \mathbf{b}_l|}{a_{max} b_{max} s_{max}^{(n)}} \tag{17}$$

As a final remark about the two proposed algorithms above, it is also important to note that CFAR detection is not performed using the estimated sparse solution ($\tilde{\mathbf{x}}$ for Algorithm 1 and $\tilde{\mathbf{X}}^{(DF)}$ for Algorithm 2), but on the contrary, sparse reconstruction is done using the CFAR detection result. Indeed, the proposed algorithms merge sparse reconstruction and CFAR detection in a new nested architecture, in which OMP provides the detection statistic, while CFAR detection threshold is used to stop OMP iterations. The input scaling of the detection statistic ($c_{max}^{(corr)}$) is obtained in our case as a consequence of its normalization by the residual norm (line 12 of Algorithm 1 and line 14 of Algorithm 2).

C. Computational complexity

Finally, the complexity of the two CD proposed algorithms has been assessed and compared to that of the corresponding Nyquist processing architectures. The results are provided in Table I and illustrated in Figure 6 for several values of M and $T_{coh} = 10$ sec. Since both CD algorithms actually stop after a number of iterations N_{iter} between 1 and N_{tg}, the complexity curves are also plotted for three N_{iter} values.

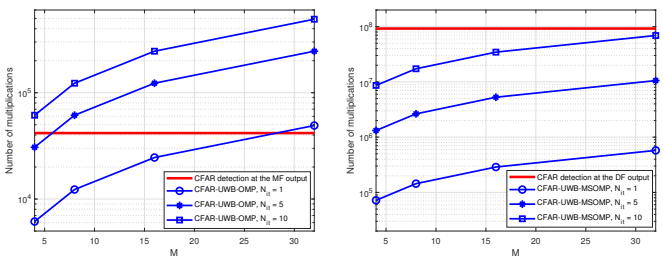

(a) (b)

Fig. 6: Complexity comparison between Nyquist and sub-Nyquist CFAR approaches for: (a) one-snapshot processing and (b) multiple-snapshots processing

As it can be noticed, the complexity of the proposed CFAR-UWB-MSOMP algorithm is reduced compared to the multiple-snapshots Nyquist processing, for all the considered values of M and N_{iter}, unlike the CFAR-UWB-OMP algorithm, which yields higher complexity in most cases. Nevertheless, it is worth noting that the main advantage of CD algorithms is actually related to the huge reduction of the sampling frequency, which is divided by N=1536 for the application considered in this paper, leading to significant gains in terms of hardware complexity and power consumption.

IV. Simulations results

The scenario considered for our simulations is shown in Fig. 7. The IR-UWB radar operates in a challenging heavy-cluttered CM7 indoor environment, whose impulse response is illustrated in Fig. 2. In this scenario, we have also considered a stationary person located at 3 m from the radar and two other fast walking and slow walking people, who are moving in front of the radar within the range intervals [2 m, 8 m] and [3.5 m, 6 m]. A Doppler frequency of $f_{stat} = 0.4$ Hz is associated to the stationary person, corresponding to a respiratory rate of 24 breaths per minute, while for the two moving people, their average velocities of 6.5 km/h = 1.8 m/s and 3 km/h = 0.83 m/s result in Doppler shifts of $f_{fast} = \frac{2v_{fast}}{\lambda_c} \cong 87$ Hz and $f_{slow} = \frac{2v_{slow}}{\lambda_c} \cong 41$ Hz, respectively. Actually, as moving people also breathe, two Doppler shifts, i.e. $f_{fast} \pm f_{stat}$ and $f_{slow} \pm f_{stat}$, should be associated with each of them, but a simplified configuration can be considered in this case, given that f_{stat} is much lower than both f_{fast} and f_{slow}.

Note that a linear motion model for the people velocity has been considered in our simulations. They initiate their movement from a standstill, quickly accelerate to reach their maximum velocity, which is then maintained constant, and decelerate rapidly at the end, before stopping and going back in the other sense. Consequently, while the Doppler shift for the stationary person can be considered as constant, a Doppler spectrum has to be rather associated to moving people.

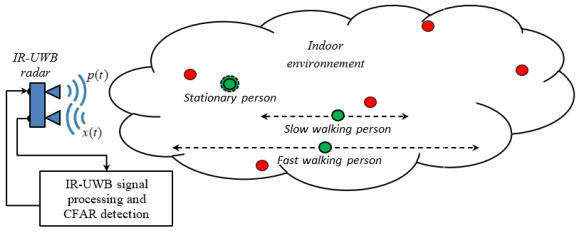

Fig. 7: Considered scenario for the simulation results

Two IR-UWB waveforms have been considered in our simulations. The first one is a frequency-shifted Gaussian pulse and is the same as for the Novelda IR-UWB radar [39], used to acquire the measured data in Section V. Its analytical expression is given below:

$$p(t) = V_{TX} \exp\left(-\frac{t^2}{2T_g^2}\right) \cos(2\pi\nu_c t) \tag{18}$$

where V_{TX} is the transmitted pulse amplitude, $T_g = (\pi B_{-10dB}\sqrt{\log_{10}(e)})^{-1}$, $\nu_c = 7.29$ GHz and $B_{-10dB} = 1.4$

TABLE I: Complexity of Nyquist and sub-Nyquist CFAR approaches

Processing approach	**Technique/Algorithm**	**Complexity**
One-snapshot processing	CFAR detection at the MF output	$\mathcal{O}(2N(log_2(N)+3))$
	CFAR-UWB-OMP	$\mathcal{O}(N_{iter}MN)$
Multi-snapshots processing	CFAR detection at the DF output	$\mathcal{O}(N(Nlog_2(N)+2N_{rec}log_2(N_{rec})))$
	CFAR-UWB-MSOMP	$\mathcal{O}(N_{iter}MN_{rec}(N_{iter}^2+8))$

GHz is the -10 dB waveform bandwidth. The second one is a specially designed waveform [40], optimized with respect to the normalized effective signal power (NESP), which is defined by:

$$NESP(p(t)) = \frac{\int |P(\nu)|^2 d\nu}{\int M_{ECC}(\nu) d\nu} \tag{19}$$

where $P(\nu)$ is the UWB waveform spectrum and $M_{ECC}(\nu)$ is the power spectral density mask defined by ECC/ETSI for the UWB emissions in Europe.

Fig. 8 shows the power spectral densities of the two UWB waveforms considered in our simulations, which comply with the ECC regulations and are characterized by $NESP_{Novelda} = 0.33$ and $NESP_{opt} = 0.74$. Thus, it is worth noting that although the Novelda waveform has the advantage of the simplicity, the signal-to-noise ratio (SNR) is improved by 3.5 dB in the case of the NESP-optimized waveform, for a given maximum Effective Isotropic Radiated Power (EIRP) level. Furthermore, the SNR gain of the matched filter is 4.8 dB and 6.9 dB for the Novelda and NESP-optimized waveforms, respectively.

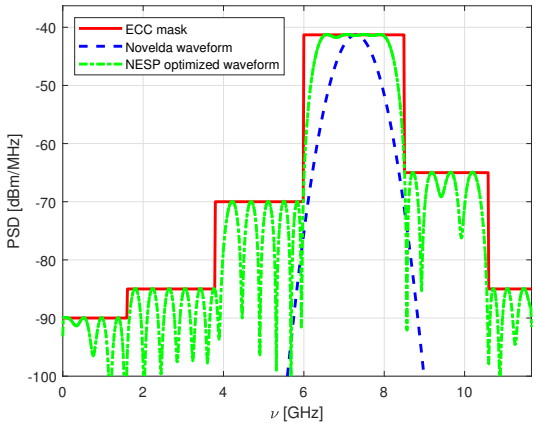

Fig. 8: Power spectral densities of the two UWB waveforms considered in our simulations.

Fig. 9 presents the noiseless and the noisy cluttered signals for an acquisition duration of 20 sec, as well as the processing results (matched filtering and Doppler focusing) at the Nyquist frequency for the considered scenario. Since the SNR gets lower as the range from the radar increases, a maximum SNR of 0 dB corresponding to the closest position is considered for our simulations. The amplitude variations of the signal of interest (SoI) for both a stationary and a moving person are explained in Appendix A.

As already mentioned in Section II, the CFAR detection is performed at MF output for moving people, resulting in

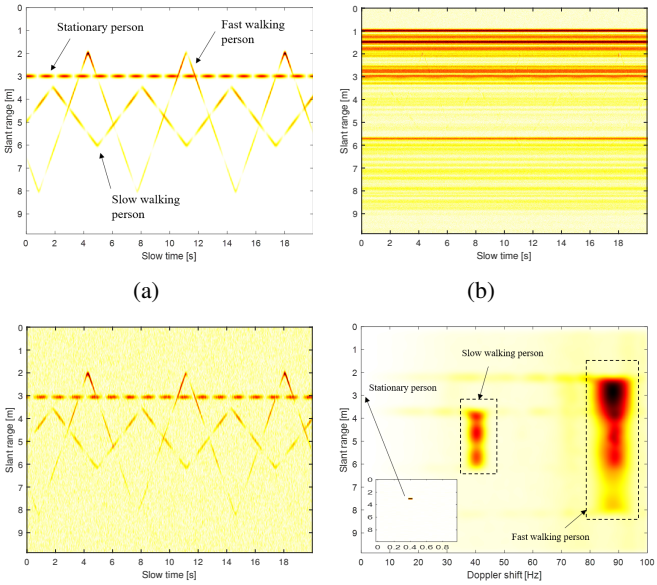

Fig. 9: Signal processing results at the Nyquist sampling frequency in the considered scenario involving two moving people and one stationary person for a maximum input SNR = 0 dB: (a) noiseless simulated SoI, (b) noisy and cluttered SoI, (c) MF output, and (d) DF output

the performance curves plotted in Fig. 10(a). The stationary person can be also detected at the MF output, with the same performance, but the detection rate is much better after the DF stage, the performance gain being proportional with the coherent integration time, as shown in Fig. 10(b) for T_{coh}=10 sec. Note that the performance curves are plotted in both cases with respect to the in-band SNR ratio at the MF input or equivalently at the whitening filter output. This choice is motivated by the possibility of directly comparing Nyquist and sub-Nyquist approaches, as well as one-snapshot against multiple snapshots signal processing options. Note also that the additional SNR gain of 3.5 dB obtained with the NESP-optimized waveform is not visible in these figures because the detection rate corresponding to the two waveforms is estimated for the same SNR values.

In the case of compressed detection, we compare not only the performance provided by the two waveforms, but also the detection rate obtained for different levels of the sensing matrix coherence. Thus, for each one of the two waveforms we consider a minimum coherence level μ_{min} corresponding to an optimized set of 4×4 FC $\left\{c_{k_m}^{(p)}\right\}_{k_m \in \mathbf{k}_M}$, and a high coherence level μ_{max}, typically associated to consecutive FC.

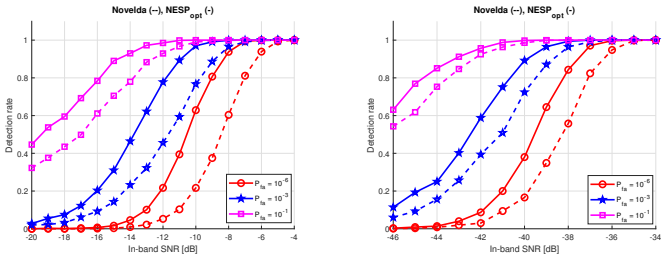

(a) (b)

Fig. 10: CFAR detection results for signal processing at the Nyquist sampling frequency: (a) at the MF output and (b) at the DF output (T_{coh}=10 sec.)

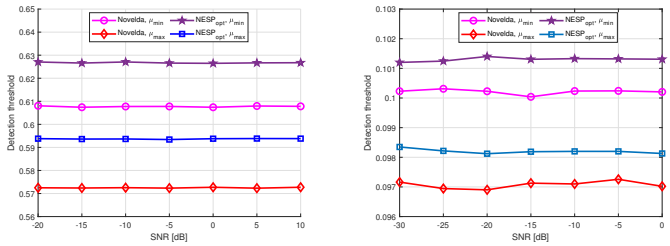

(a) (b)

Fig. 12: Detection threshold variation for CFAR CD, with P_{fa} = 0.1 and using: (a) CFAR-UWB-OMP and (b) CFAR-UWB-MSOMP

The optimized FC sets for the two UWB waveforms are shown in Fig. 11. Note that the minimum coherence value is $\mu_{min} = 0.89$ for the Novelda pulse and $\mu_{min} = 0.76$ for the NESP-optimized pulse, while the μ_{max} values are very close, i.e. 0.99 and 0.98, respectively.

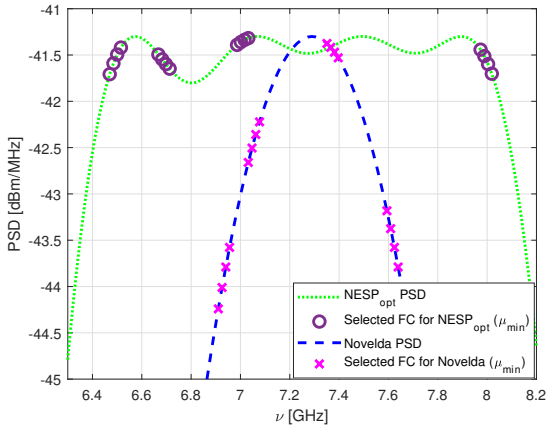

Fig. 11: Optimized FC sets for minimum coherence in the case of the two UWB waveforms considered in our simulations

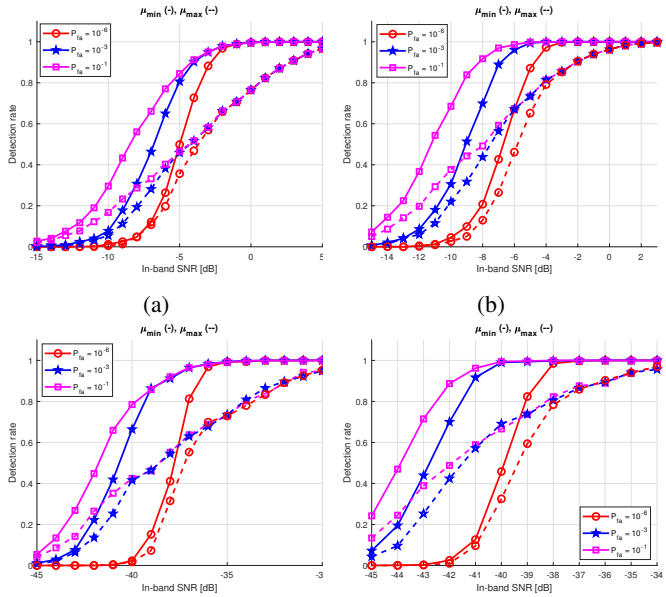

(a) (b) (c) (d)

Fig. 13: Impact of the coherence on the CFAR CD performance using: (a) CFAR-UWB-OMP and Novelda waveform, (b) CFAR-UWB-OMP and NESP-optimized waveform, (c) CFAR-UWB-MSOMP and Novelda waveform, and (d) CFAR-UWB-MSOMP and NESP-optimized waveform

As stated in Section III and illustrated by Fig. 12 for $P_{fa} = 0.1$, whether the decision is taken using CFAR-UWB-OMP (one-snapshot processing) or CFAR-UWB-MSOMP (multi-snapshots processing), the detection threshold is invariant with respect to the noise power and depends only on the UWB waveform shape and sensing matrix coherence.

The impact of the coherence on the detection performance, for both CFAR-UWB-OMP and CFAR-UWB-MSOMP algorithms, is illustrated in Fig. 13. Note that the same value of T_{coh}=10 sec has been used for the DF as in the case of Nyquist processing. It can be readily seen that lower the coherence values, the better the detection performance and that for the highest coherence levels, the values of interest for the detection rate (higher than 0.8) do not increase anymore with the false alarm probability. The most important SNR gain for both UWB waveforms is obtained for $P_{fa} = 0.1$ and it is of about 5dB, at a detection rate level $P_{det} = 0.8$. In Fig. 14 we also compare the CFAR CD performance of the two UWB waveforms, for both moving and stationary people. We now focus only on the most interesting configuration, associated to the lowest coherence level (μ_{min}). The comparison results are roughly similar to those shown in Fig. 10, except that as the false alarm level varies, the SNR gain of NESP-optimized over Novelda waveform, which is almost constant in the case of Nyquist processing, becomes more significant for higher P_{fa} values in the compressed detection case. It reaches over 3 dB for P_{fa}= 0.1 and P_{det}= 0.8, compared to 2 dB and 1 dB, at the MF and DF output, respectively, in the case of Nyquist processing. Finally, an SNR loss depending of the false alarm level can be also noticed in the case of compressed detection compared to the Nyquist processing. For the considered P_{fa} values, this performance loss is more significant for moving human detection (up to 6 dB) than for the stationary human detection (up to 4 dB).

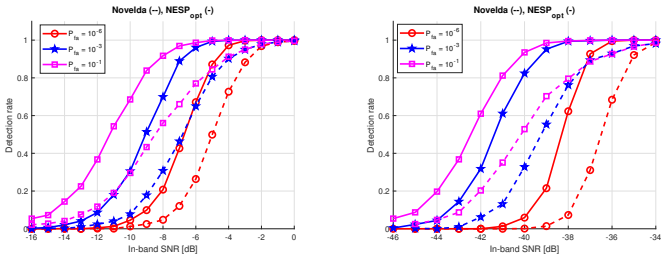

(a) (b)

Fig. 14: Impact of the UWB waveform on the CFAR CD performance, for the lowest coherence level (μ_{min}), using: (a) CFAR-UWB-OMP and (b) CFAR-UWB-MSOMP

V. Experimental results

This section presents the experimental results using compressed CFAR processing for detecting people in the Industry 4.0 indoor environment at the University of Brest. The experimental setup, shown in Fig. 15, includes a drug industrial production chain with associated supervision and cybersecurity infrastructure. During our experiments, the platform was operational, so the Doppler spectrum generated by its mobile components and conveyors, as well as the signal backscattered by its rigid structure, are mixed with the signal of interest (SoI) backscattered by a person present in the room. Xethru X4M03 IR-UWB Novelda radars have been used in our experiments, with parameters outlined in Table II from the datasheet [41].

Each radar was connected to a laptop for data storage and analysis, utilizing MATLAB® software for data processing.

Three scenarios were investigated to evaluate UWB human detection in indoor environments and to assess the effectiveness of the proposed approach:

- Scenario 1: A person sits approximately 4 meters from the UWB radar for 60 seconds.
- Scenario 2: A person walks slowly or quickly in front of the UWB radar for 60 seconds.
- Scenario 3: A person alternates between sitting at about 4 meters and 5.2 meters, with periods of slow or fast walking, for 120 seconds.

TABLE II: Main parameters of X4M03 IR-UWB Novelda radar

Parameter	Value
Power consumption	120 mW
Center frequency ν_c	7.29 GHz
Fast-time acquisition duration T_r	65.844 ns
Frames per second(FPS)	200 Hz
Detection zone	0.8 - 9.5 m
Bandwidth at -10 dB	1.4 GHz
Duty cycle	0.95
Antenna beamwidth	65° azimuth and elevation

Fig. 16 presents signal processing results for the first scenario. Fig. 16(a) shows signal envelopes revealing a cluttered indoor environment challenging for person detection. The IR-UWB radar avoids interference by blocking reception for the first 5.33 ns of PRI (0.8 meters range). After applying MTI and whitening filters, Fig. 16(b) displays improved clutter removal, enabling OMP reconstruction using the CFAR-UWB-OMP algorithm with a zero threshold. CFAR detection results for $P_{fa} = 10^{-1}$ and $P_{fa} = 10^{-6}$ are shown in Fig. 16(c) and (d), respectively, clearly indicating a seated person with identifiable breathing patterns. Fig. 16(e) demonstrates enhanced localization in the range-Doppler plane through Doppler focusing and sparse reconstruction using matrix sketching OMP. Finally, Fig. 16(f) exhibits the output of the CFAR-UWB-MSOMP algorithm, accurately extracting the person's position and breathing rate. Note that algorithms outputs have been convolved with a Hamming window for clarity.

Fig. 17 depicts results from two scenarios: a person walking slowly (Fig. 17(a), (c), (e), and (g)) and quickly (Fig. 17(b), (d), (f), and (h)) in front of a UWB radar. Trajectories are clear after sparse reconstruction and CFAR detection. Doppler spectrums in Fig. 17(g) and (h) correlate with motion patterns, showing ranges of 2.2 to 4.2 meters for slow walking and 2.2 to 5.2 meters for fast walking. These Doppler shifts correspond to speeds of 0 to 1.6 km/h and 0 to 5 km/h respectively. Machine learning techniques can further analyze these patterns to distinguish people from other objects. Doppler focusing and sparse reconstruction reveal significant amplitudes beyond the walking zone, primarily due to indoor clutter. Additionally, when the person walks between the radar and a wall 6.5 meters away (seen in Fig. 17(a) and (b)), her body intermittently blocks the signal to the wall, causing signal fluctuations. This creates a notable amplitude peak at 6.5 meters after Doppler focusing.

The final experiment is more elaborate, with a data acquisition period of 120 seconds. During this time, the person alternates between sitting and moving alongside the industrial platform. The experiment consists of four distinct phases:

1) The person sits about 5.2 meters away from the radar for 50 seconds.
2) The person slowly moves back and forth within the range of 2 to 5.2 meters for 20 seconds.
3) The person sits again, this time about 4 meters away, for 30 seconds.
4) The person walks faster than in the second phase for the last 20 seconds.

Fig. 18 shows the signal processing results. The CFAR-UWB-OMP algorithm (Fig. 18(c)) clearly identifies the four phases with a false alarm level of $P_{fa} = 10^{-6}$. Doppler focusing and sparse reconstruction results are shown in Figure 18(d) for Doppler shifts above 1 Hz, and in Fig. 18(e) and Fig. 18(f) for shifts up to 1 Hz. This separation enhances readability as amplitude peaks are higher when the person is stationary, making moving objects less visible. Fig. 18(d) highlights three Doppler spectrum zones: one common to both motion phases, and two corresponding to slow and fast walking. Fig. 18(f) displays the CFAR-UWB-MSOMP algorithm output, detecting and identifying the person's breathing rate during seated intervals with the same false alarm level. Two peaks at 4 meters and 5.5 meters correspond to a Doppler shift of about 0.5 Hz.

Despite the second sitting position being closer, both amplitudes are similar due to a higher processing gain for the first position, which has a longer coherent integration time

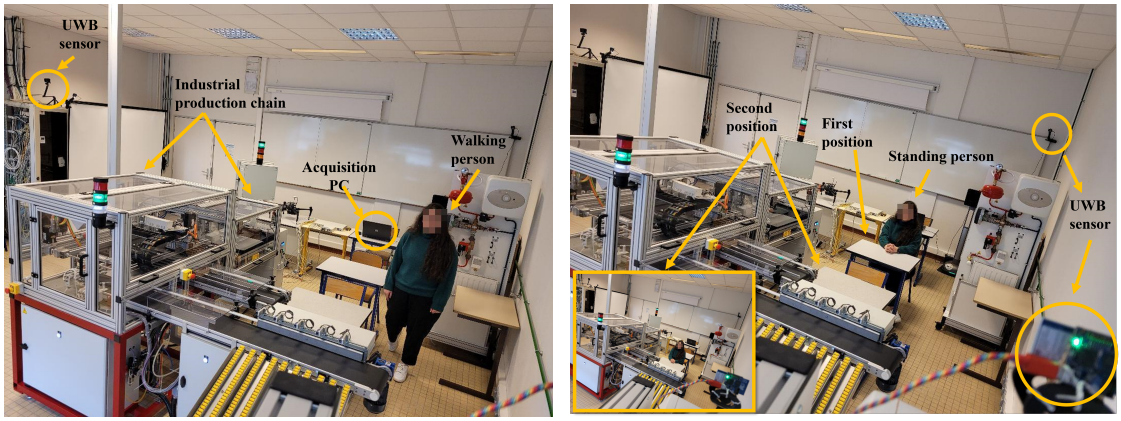

(a) (b)

Fig. 15: Experimental setup in the industrial platform used for data acquisition, illustrating the two main phases of the scenarios: (a) person walking in front of the radar, and (b) person sitting

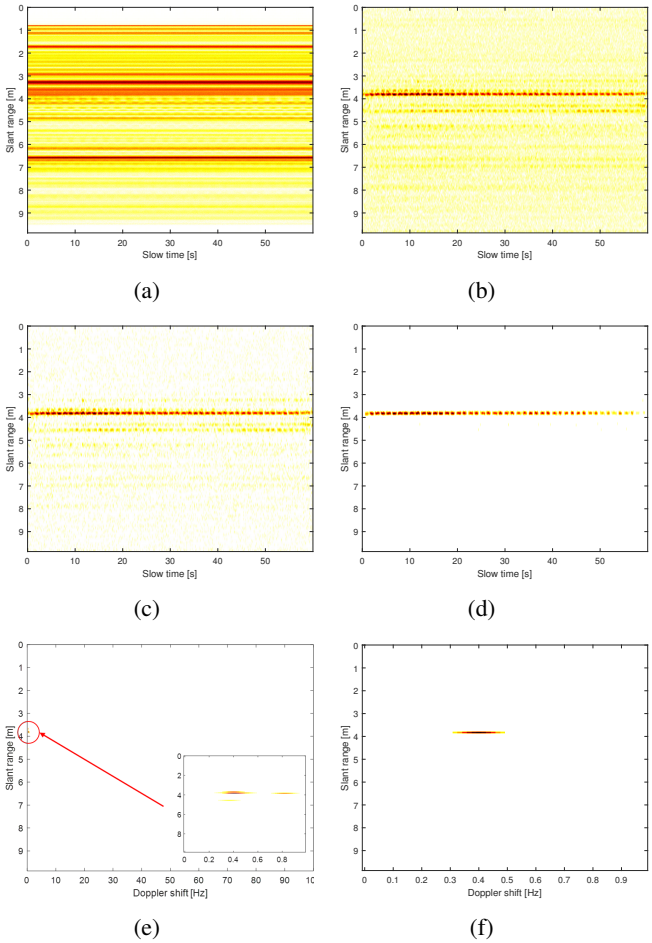

(a) (b) (c) (d) (e) (f)

Fig. 16: Signal processing results for the first considered scenario (person sitting in front of the IR-UWB radar): (a) measured data, (b) OMP reconstruction (c) CFAR-UWB-OMP output ($P_{fa} = 10^{-1}$), (d) CFAR-UWB-OMP output ($P_{fa} = 10^{-6}$), (e) Doppler focusing and matrix sketching OMP reconstruction, (f) CFAR-UWB-MSOMP output ($P_{fa} = 10^{-6}$)

(50 seconds vs. 30 seconds). A third peak results from a constructive multipath summing in phase with the second breathing signal.

VI. Conclusion

We have described a comprehensive approach to compressed CFAR human detection, in highly cluttered indoor environments, using IR-UWB radar. Although it shares some aspects with other related research, to the best of our knowledge, it is the first time that the compressed sensing and CFAR detection are jointly considered for smart factory indoor applications.

The two newly proposed OMP-based sparse reconstruction and CFAR detection algorithms have been designed to undertake both stationary and moving people extraction from heavy-cluttered signals, sampled at a rate much lower than the Nyquist limit. Another important contribution has been represented by Xampling scheme optimization for both minimizing sensing matrix coherence, while keeping reduced its hardware complexity. In this way, we have not only enhanced the detection rates, but also paved the way for more efficient implementation of CS techniques in practical scenarios. Furthermore, we have proposed an effective detection statistic, making the detection threshold invariant to the noise power, and identified the corresponding best-fitted distribution, which has been validated by statistical tests.

The extensive performance analysis of the proposed algorithms, using both simulated and measured data, for several canonical scenarios, is also worth to be mentioned as a significant contribution. We have demonstrated the effectiveness of our compressed CFAR approach for human detection, particularly in Industry 4.0 indoor environments. This validation underscores its potential to offer robust and reliable performance in such complex use cases.

Although the two proposed CD algorithms have the CFAR property, only their general principle relying on the Neyman-Pearson optimal test is provided in the paper. Further research is necessary to design a true CFAR detector taking into account all the practical implementation constraints. Since a

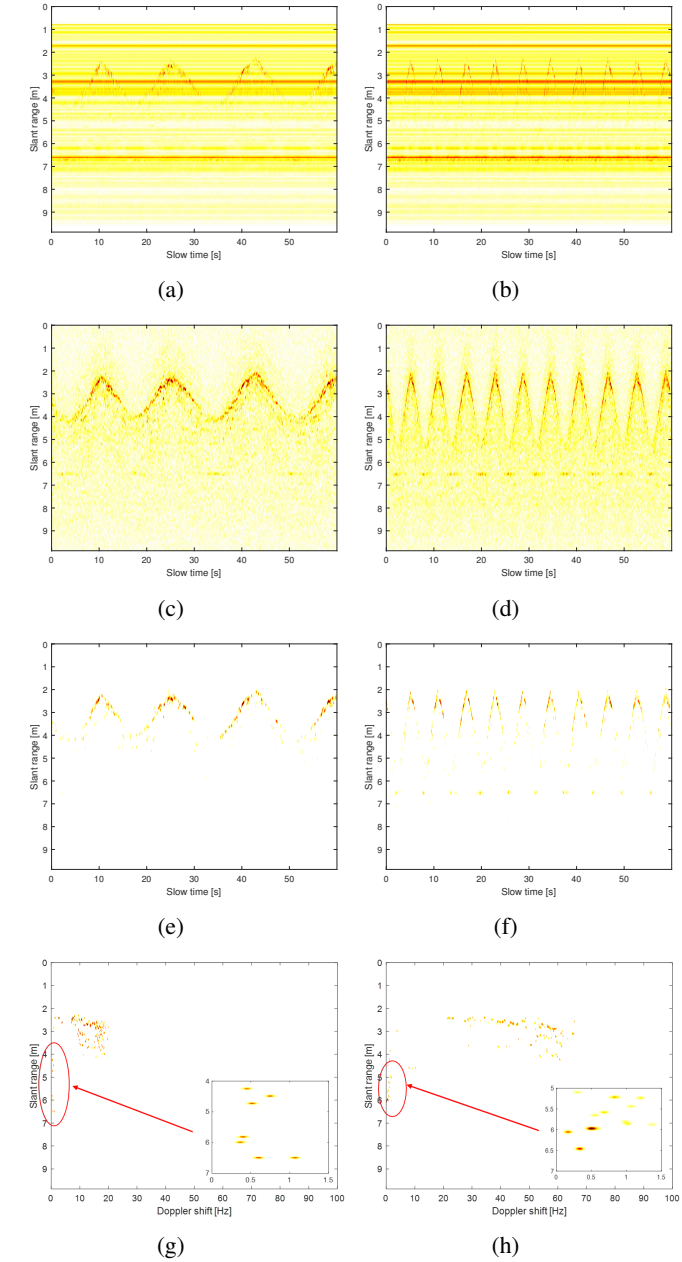

Fig. 17: Signal processing results for the second considered scenario (person walking slowly/quickly in front of the IR-UWB radar): (a) and (b) measured data , (c) and (d) OMP reconstruction, (e) and (f) CFAR-UWB-OMP output ($P_{fa} = 10^{-6}$), (g) and (h) Doppler focusing and matrix sketching OMP reconstruction

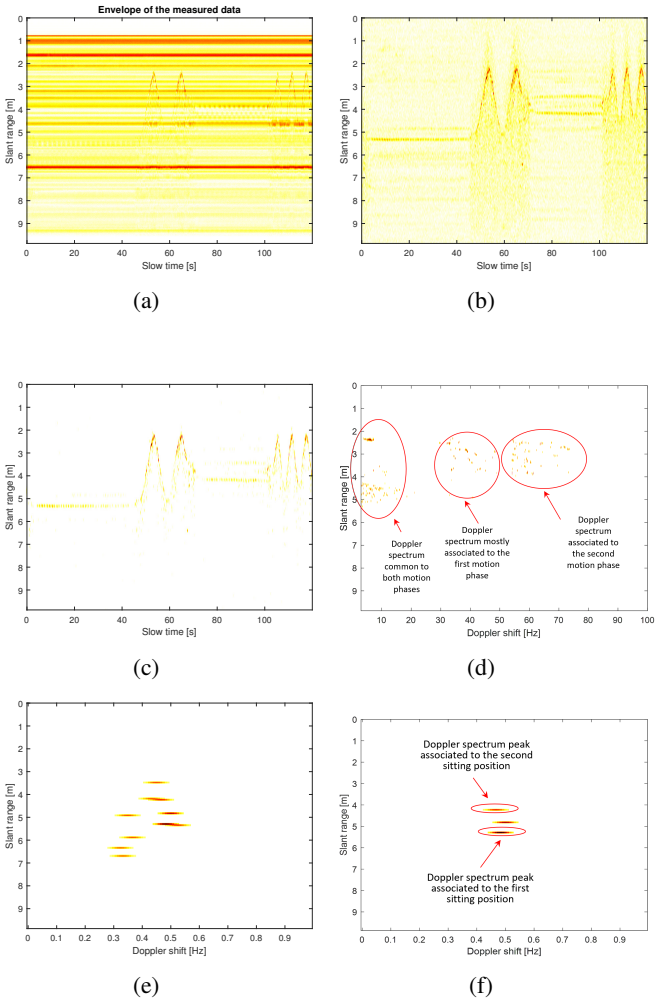

Fig. 18: Signal processing results for the third considered scenario (person alternating seated positions with slow/fast walking phases): (a) measured data, (b) OMP reconstruction, (c) CFAR-UWB-OMP output ($P_{fa} = 10^{-6}$), (d) Doppler focusing and sparse reconstruction above 1 Hz, (e) Doppler focusing and sparse reconstruction below 1 Hz, (f) CFAR-UWB-MSOMP output below 1 Hz ($P_{fa} = 10^{-6}$)

wide variety of CFAR detectors can be combined with sparse reconstructors to form the proposed compressed detection algorithms, we plan to carry out their comparative analysis as future work, including their capability to operate in the presence of clutter edges. We also plan to rely on the detection results to perform people tracking and to thoroughly investigate the Doppler signature analysis for human detection, employing specific machine learning techniques. This exploration aims to differentiate between human movements and other objects within intricate environments, thereby advancing the capabilities of our detection system in complex and dynamic settings.

ACKNOWLEDGMENT

This work is supported in part by the European Regional Development Fund (ERDF), the French Ministry of Higher Education and Research, the Brittany Region, Brest Métropole, the departmental council 29 through the CPER projects "SpaceTechDroneTech" and "Industrie du Futur".

REFERENCES

[1] X. Liang, J. Deng, H. Zhang, and T. A. Gulliver, "Ultra-Wideband Impulse Radar Through-Wall Detection of Vital Signs," *Scientific Reports*, vol. 8, no. 1, p. 13367, Sep. 2018.

[2] S. D. Liang, "Sense-through-wall human detection based on UWB radar sensors," *Signal Processing*, vol. 126, pp. 117–124, Sep. 2016.

[3] J. W. Choi, D. H. Yim, and S. H. Cho, "People Counting Based on an IR-UWB Radar Sensor," *IEEE Sensors Journal*, vol. 17, no. 17, pp. 5717–5727, Sep. 2017.

[4] M. Cheraghinia, A. Shahid, S. Luchie, G.-J. Gordebeke, O. Caytan, J. Fontaine, B. Van Herbruggen, S. Lemey, and E. De Poorter, "A comprehensive overview on UWB radar: Applications, standards, signal processing techniques, datasets, radio chips, trends and future research directions," *arXiv preprint arXiv:2402.05649*, 2024.

[5] Z. Li, Q. An, F. Qi, F. Liang, H. Lv, Y. Zhang, X. Yu, and J. Wang, "Detection of People Trapped under the Ruins Using Dual-frequency IR-UWB Radar," in *2018 15th European Radar Conference (EuRAD)*. IEEE, Sep. 2018, pp. 83–86.

[6] T. G. Savelyev, X. Zhuge, B. Yang, A. G. Yarovoy, L. P. Ligthart, M. Drozdov, and B. Levitas, "Development of UWB microwave array radar for concealed weapon detection," *11-th International Radar Symposium*, pp. 1–4, 2010. [Online]. Available: https://api.semanticscholar.org/CorpusID:38300821

[7] D.-H. Kim, "Lane detection method with impulse radio ultra-wideband radar and metal lane reflectors," *Sensors*, vol. 20, no. 1, 2020. [Online]. Available: https://www.mdpi.com/1424-8220/20/1/324

[8] S. Shyam, S. Juliet, and K. Ezra, "Vehicle Monitoring and Localization using UWB in Complex Parking Lot," in *2022 International Conference on Sustainable Computing and Data Communication Systems (ICSCDS)*. Erode, India: IEEE, Apr. 2022, pp. 937–943.

[9] T. Lauteslager, M. Tommer, T. S. Lande, and T. G. Constandinou, "Coherent UWB radar-on-chip for in-body measurement of cardiovascular dynamics," *IEEE Transactions on Biomedical Circuits and Systems*, vol. 13, no. 5, pp. 814–824, 2019.

[10] T. Lauteslager, M. Tommer, K. G. Kjelgård, T. S. Lande, and T. G. Constandinou, "Intracranial heart rate detection using UWB radar," in *2016 IEEE Biomedical Circuits and Systems Conference (BioCAS)*, 2016, pp. 119–122.

[11] F. Khan, S. Azou, R. Youssef, P. Morel, E. Radoi, and O. A. Dobre, "An IR-UWB multi-sensor approach for collision avoidance in indoor environments," *IEEE Transactions on Instrumentation and Measurement*, vol. 71, pp. 1–13.

[12] Liuqing Yang and G. Giannakis, "Ultra-wideband communications - An idea whose time has come," *IEEE Signal Processing Magazine*, vol. 21, no. 6, pp. 26–54, Nov. 2004.

[13] Y. Eldar and G. Kutyniok, Eds., *Introduction to compressed sensing*. Cambridge University Press, 2012, pp. 1–64.

[14] M. Mishali and Y. C. Eldar, "From Theory to Practice: Sub-Nyquist Sampling of Sparse Wideband Analog Signals," *IEEE Journal of Selected Topics in Signal Processing*, vol. 4, no. 2, pp. 375–391, 2010. [Online]. Available: https://ieeexplore.ieee.org/document/5419072/

[15] G. Burel, E. Radoi, R. Gautier, and D. Le Jeune, "Wideband Spectrum Sensing Using Modulated Wideband Converter and Data Reduction Invariant Algorithms," *Sensors*, vol. 23, no. 4, p. 2263. [Online]. Available: https://www.mdpi.com/1424-8220/23/4/2263

[16] I. Maravic and M. Vetterli, "Sampling and reconstruction of signals with finite rate of innovation in the presence of noise," *IEEE Transactions on Signal Processing*, vol. 53, no. 8, pp. 2788–2805, Aug. 2005.

[17] E. Baransky, G. Itzhak, N. Wagner, I. Shmuel, E. Shoshan, and Y. Eldar, "Sub-Nyquist radar prototype: Hardware and algorithm," *IEEE Transactions on Aerospace and Electronic Systems*, vol. 50, no. 2, pp. 809–822, 2014.

[18] A. De Maio, Y. Eldar, and A. Haimovich, *Compressed sensing in radar signal processing*. United Kingdom: Cambridge University Press, Jan. 2019, publisher Copyright: © Cambridge University Press 2020.

[19] K. Gedalyahu, R. Tur, and Y. C. Eldar, "Multichannel sampling of pulse streams at the rate of innovation," *IEEE Transactions on Signal Processing*, vol. 59, no. 4, pp. 1491–1504, 2011.

[20] Z. Wei, J. Zhang, Z. Xu, Y. Liu, and K. Okarma, "Measurement Matrix Optimization via Mutual Coherence Minimization for Compressively Sensed Signals Reconstruction," *Mathematical Problems in Engineering*, vol. 2020, pp. 1–18, 2020. [Online]. Available: https://onlinelibrary.wiley.com/doi/abs/10.1155/2020/7979606

[21] C. Rusu and N. González-Prelcic, "Optimized Compressed Sensing via Incoherent Frames Designed by Convex Optimization," Nov. 2016. [Online]. Available: http://arxiv.org/abs/1507.02454

[22] K. Ardah, M. Pesavento, and M. Haardt, "A Novel Sensing Matrix Design for Compressed Sensing via Mutual Coherence Minimization," in *2019 IEEE 8th International Workshop on Computational Advances in Multi-Sensor Adaptive Processing (CAMSAP)*. Le gosier, Guadeloupe: IEEE, 2019, pp. 66–70. [Online]. Available: https://ieeexplore.ieee.org/document/9022467/

[23] T. Yaacoub, O. A. Dobre, R. Youssef, and E. Radoi, "Optimal Selection of Fourier Coefficients for Compressed Sensing-Based UWB Channel Estimation," *IEEE Wireless Communications Letters*, vol. 6, no. 4, pp. 466–469. [Online]. Available: http://ieeexplore.ieee.org/document/7927744/

[24] A. F. Molisch, "Ultra-Wide-Band Propagation Channels," *Proceedings of the IEEE*, vol. 97, no. 2, pp. 353–371, Feb. 2009.

[25] A. Ghorbani, S. M. Karbasi, and M. M. Nayebi, "A genetic approach to MTI filter design with nonuniform sampling," in *2020 IEEE Radar Conference (RadarConf20)*, 2020, pp. 1–6.

[26] T. Cai and L. Wang, "Orthogonal matching pursuit for sparse signal recovery with noise." *IEEE Transactions on Information Theory*, vol. 57, pp. 4680–4688, 01 2011.

[27] B. Mamandipoor, D. Ramasamy, and U. Madhow, "Newtonized orthogonal matching pursuit: Frequency estimation over the continuum," *CoRR*, vol. abs/1509.01942, 2015. [Online]. Available: http://arxiv.org/abs/1509.01942

[28] J. Zhu, L. Han, R. S. Blum, and Z. Xu, "Multi-snapshot newtonized orthogonal matching pursuit for line spectrum estimation with multiple measurement vectors," *Signal Processing*, vol. 165, pp. 175–185, 2019. [Online]. Available: https://www.sciencedirect.com/science/article/pii/S0165168419302658

[29] J. Tropp, "Greed is good: algorithmic results for sparse approximation," *IEEE Transactions on Information Theory*, vol. 50, no. 10, pp. 2231–2242, 2004.

[30] M. Xu, J. Zhu, J. Fang, N. Zhang, and Z. Xu, "Cfar based nomp for line spectral estimation and detection," 2022.

[31] R. Baraniuk, M. Davenport, R. DeVore, and M. Wakin, "A Simple Proof of the Restricted Isometry Property for Random Matrices," *Constructive Approximation*, vol. 28, no. 3, pp. 253–263, Dec. 2008.

[32] E. J. Candes, Y. C. Eldar, D. Needell, and P. Randall, "Compressed Sensing with Coherent and Redundant Dictionaries," *Applied and Computational Harmonic Analysis*, vol. 31, no. 1, pp. 59–73, 2011.

[33] T. Yaacoub, R. Youssef, E. Radoi, and G. Burel, "Low complexity FRI based sampling scheme for UWB channel estimation," in *2016 24th European Signal Processing Conference (EUSIPCO)*. IEEE, 2016, pp. 657–661. [Online]. Available: http://ieeexplore.ieee.org/document/7760330/

[34] M. A. Richards, *Fundamentals of Radar Signal Processing*, 2nd ed. New York: McGraw-Hill Education, 2014.

[35] L. de Haan and A. Ferreira, *Extreme Value Theory: An Introduction*, ser. Springer Series in Operations Research and Financial Engineering. Springer New York, 2007.

[36] D. Castro-Camilo, R. Huser, and H. Rue, "Practical strategies for generalized extreme value-based regression models for extremes," *Environmetrics*, vol. 33, no. 6, p. e2742, 2022.

[37] S. Coles, *An Introduction to Statistical Modeling of Extreme Values*, ser. Springer Series in Statistics. Springer, 2001. [Online]. Available: https://books.google.fr/books?id=2nugUEaKqFEC

[38] T. Wimalajeewa, Y. C. Eldar, and P. K. Varshney, "Recovery of sparse matrices via matrix sketching," *ArXiv*, vol. abs/1311.2448, 2013.

[39] N. Andersen, K. Granhaug, J. A. Michaelsen, S. Bagga, H. A. Hjortland, M. R. Knutsen, T. S. Lande, and D. T. Wisland, "A 118-mW Pulse-Based Radar SoC in 55-nm CMOS for Non-Contact Human Vital Signs Detection," *IEEE Journal of Solid-State Circuits*, vol. 52, no. 12, pp. 3421–3433, 2017. [Online]. Available: https://ieeexplore.ieee.org/document/8106658/

[40] A. Amini, P. Mohajerin Esfahani, M. Ghavami, and F. Marvasti, "UWB orthogonal pulse design using Sturm–Liouville boundary value problem," *Signal Processing*, vol. 159, pp. 147–158.

[41] X4 - Datasheet by Novelda, "X4m03 datasheet," Novelda, Tech. Rep., 2017. [Online]. Available: https://novelda.com/wp-content/uploads/2023/03/x4_datasheet_RevA.pdf

APPENDIX A

Let us consider the analytic signal in (1) corresponding to only one target, under the hypothesis that the associated Doppler shift is constant, i.e.$f_l^{(q)} = f_D$, during the acquisition time:

$$\begin{aligned} r_q(t) &= \sigma^{(q)} p(t - \tau^{(q)} - qT_{rec}) e^{j2\pi f_D q T_{rec}}, \\ & t \in [qT_{rec}, qT_{rec} + T_r], q = 0, \ldots, N_{rec} - 1 \end{aligned} \tag{A-1}$$

When this signal is sampled at the Nyquist rate $\{t_{n,q} = n/F_{Nyq} + qT_{rec}\}_{n=0,\ldots,N-1, q=0,\ldots,N_{rec}-1}$, the following data matrix is obtained from (A-1) and (18):

$$\begin{aligned} & z(n,q) = \text{Re}\{\sigma^{(q)} p\big(n/F_{Nyq} - \tau^{(q)}\big) e^{j2\pi(f_D/F_{rec})q}\} = \\ & \sigma^{(q)} V_{Tx} e^{-\frac{\left(n/F_{Nyq} - \tau^{(q)}\right)^2}{2T_g^2}} \cos\big(2\pi\big(\nu_c(n/F_{Nyq} - \tau^{(q)}) + \\ & (f_D/F_{rec})q\big)\big), \\ & n = 0, \ldots, N-1, q = 0, \ldots, N_{rec} - 1 \end{aligned} \tag{A-2}$$

If the target delays are taken only on the data grid, i.e. $\tau_l^{(q)} = n^{(q)}/F_{Nyq}$, then for the range cell $n^{(q)}$ and the q^{th} PRI, we get:

$$\begin{aligned} & z(n^{(q)}, q) = \sigma^{(q)} V_{Tx} \cos\big(2\pi\big(f_D/F_{rec})q\big), \\ & q = 0, \ldots, N_{rec} - 1 \end{aligned} \tag{A-3}$$

In the equation above, the term $\cos\big(2\pi\big(f_D/F_{rec})q\big)$, depending on the target Doppler shift, explains the amplitude fluctuations of the simulated data matrix represented in Fig. 9(a). In a similar way, relying on (A-1) and (4), the corresponding data matrix after the MTI processing can be then written in the form:

$$\begin{aligned} & z^{(MTI)}(n,q) = \text{Re}\{\sigma^{(q)} p\big(n/F_{Nyq} - \tau^{(q)}\big) e^{j2\pi(f_D/F_{rec})q} - \\ & \sigma^{(q-1)} p\big(n/F_{Nyq} - \tau^{(q-1)}\big) e^{j2\pi(f_D/F_{rec})(q-1)}\}, \\ & n = 0, \ldots, N-1, q = 1, \ldots, N_{rec} - 1 \end{aligned} \tag{A-4}$$

Assuming that the target reflectivity does not vary during T_{rec} , i.e. $\sigma^{(q)} = \sigma^{(q-1)}$, we get:

$$\begin{aligned} & z^{(MTI)}(n,q) = \sigma^{(q)} \text{Re}\{\big(p\big(n/F_{Nyq} - \tau^{(q)}\big) \\ & - p\big(n/F_{Nyq} - \tau^{(q-1)}\big) e^{-j2\pi(f_D/F_{rec})} \big) \\ & e^{j2\pi(f_D/F_{rec})q}\}, \\ & n = 0, \ldots, N-1, q = 1, \ldots, N_{rec} - 1 \end{aligned} \tag{A-5}$$

In the case of a stationary target, i.e. $\tau^{(q)} = \tau^{(q-1)}$, (A-5) takes the following form for the range cell $n^{(q)}$ and the q^{th} PRI:

$$\begin{aligned} & z^{(MTI)}(n^{(q)}, q) = \sigma^{(q)} V_{Tx} \text{Re}\{\big(1 - e^{-2j\pi(f_D/F_{rec})}\big) \\ & e^{2j\pi(f_D/F_{rec})q}\} = 2\sigma^{(q)} V_{Tx} \sin\big(\pi(f_D/F_{rec})\big) \\ & \text{Re}\{je^{-j\pi(f_D/F_{rec})} e^{2j\pi(f_D/F_{rec})q}\} \\ & \Rightarrow z^{(MTI)}(n^{(q)}, q) = 2\sigma^{(q)} V_{Tx} \sin\big(\pi(f_D/F_{rec})\big) \\ & \cos\big(2\pi(f_D/F_{rec})q - \pi(f_D/F_{rec}) + \pi/2\big), \\ & q = 1, \ldots, N_{rec} - 1 \end{aligned} \tag{A-6}$$

It can be noticed that the term $\cos\big(2\pi(f_D/F_{rec})q - \pi(f_D/F_{rec}) + \pi/2\big)$ yields the same slow-time amplitude fluctuations as for the data matrix, but they are phase shifted. For low values of f_D, this phase shift is of about $\pi/2$, while it is null for $f_D = F_{rec}/2$. It can be also noticed that the additional amplitude term $\sin\big(\pi(f_D/F_{rec})\big)$ has a strong impact on the SNR, especially for low Doppler shifts associated to human breathing. The role of the whitening filter is to compensate this effect, while the matched filter maximizes the SNR, resulting in Fig. 9(c).

In the case of a moving target, let us consider, without any loss of generality, a positive Doppler shift $f_D = 2\nu_r/\lambda_c$, which results in:

$$\tau^{(q)} = \tau^{(q-1)} - (2\nu_r T_{rec}/c) = \tau^{(q-1)} - f_D/(\nu_c F_{rec}) \tag{A-7}$$

Consequently, for the range cell $n^{(q)}$ and the qth PRI, (A-5) becomes:

$$\begin{aligned} & z^{(MTI)}(n^{(q)}, q) = \sigma^{(q)} \text{Re}\Big\{\big(p(0) - p(f_D/(\nu_c F_{rec}))\big) \\ & e^{-2j\pi(f_D/F_{rec})}\big) e^{2j\pi(f_D/F_{rec})q}\Big\} \\ & = \sigma^{(q)} V_{Tx} \text{Re}\Big\{\Big(1 - e^{-(f_D/(\sqrt{2}\nu_c F_{rec} T_g))^2} e^{j2\pi(f_D/F_{rec})} \\ & e^{-j2\pi(f_D/F_{rec})}\Big) e^{j2\pi(f_D/F_{rec})q}\Big\} \\ & \Rightarrow z^{(MTI)}(n^{(q)}, q) = \sigma^{(q)} V_{Tx}\Big(1 - e^{-(f_D/(\sqrt{2}\nu_c F_{rec} T_g))^2}\Big) \\ & \cos(2\pi(f_D/F_{rec})q), q = 1, \ldots, N_{rec} - 1 \end{aligned} \tag{A-8}$$

The same slow-time amplitude fluctuations as in the case of the simulated data matrix, represented by the term $\cos(2\pi(f_D/F_{rec})q)$, can be observed in this case. Indeed, as illustrated by Fig. 9(c), contrarywise to the stationary targets, for moving targets there is no phase shift between the amplitude fluctuations of the simulated and MF output data matrices. The additional amplitude term $\Big(1 - e^{-(f_D/(\sqrt{2}\nu_c F_{rec} T_g))^2}\Big)$ is zero for fixed targets with no Doppler shift, while it increases rapidly as f_D is getting larger.

APPENDIX B

We will evaluate below the coherence of the equivalent $MN_{rec} \times NN_{rec}$ sensing matrix $\mathbf{A}_{ech} = \mathbf{A} \otimes \mathbf{I}_{N_{rec}}$:

$$\begin{aligned} \mathbf{A}_{ech} &= \begin{bmatrix} a_{11}\mathbf{I}_{N_{rec}} & a_{12}\mathbf{I}_{N_{rec}} & \cdots & a_{1N}\mathbf{I}_{N_{rec}} \\ a_{21}\mathbf{I}_{N_{rec}} & a_{22}\mathbf{I}_{N_{rec}} & \cdots & a_{2N}\mathbf{I}_{N_{rec}} \\ \vdots & \vdots & \ddots & \vdots \\ a_{M1}\mathbf{I}_{N_{rec}} & a_{M2}\mathbf{I}_{N_{rec}} & \cdots & a_{MN}\mathbf{I}_{N_{rec}} \end{bmatrix} \\ &= [\mathbf{a}_1 \otimes \mathbf{I}_{N_{rec}} \ \mathbf{a}_2 \otimes \mathbf{I}_{N_{rec}} \ \ldots \ \mathbf{a}_N \otimes \mathbf{I}_{N_{rec}}] \end{aligned} \tag{B-1}$$

Let $\mathbf{a}_k^{(N_{rec})}$ denote the $MN_{rec} \times 1$ vector obtained by up-sampling $\mathbf{a}_k$ with the factor N_{rec}, i.e. having only zero components except for $a_{k,(i-1)N_{rec}+1}^{(N_{rec})}$, $i = 1, \ldots, M$. Let also denote by $\underset{\sim}{\mathbf{A}}_k = circ(\mathbf{a}_k^{(N_{rec})}) = \mathbf{a}_k \otimes \mathbf{I}_{N_{rec}}$ the $MN_{rec} \times N_{rec}$

circulant matrix associated to $\mathbf{a}_k^{(N_{rec})}$. (B1) can be then rewritten as:

$$\mathbf{A}_{ech} = [\underset{\sim}{\mathbf{A}}_1 \underset{\sim}{\mathbf{A}}_2 \dots \underset{\sim}{\mathbf{A}}_N] \tag{B-2}$$

and it is straightforward to note that:

$$\|\underset{\sim}{\mathbf{A}}_k(:,i)\| = \|\mathbf{a}_k\|, i = 1, \dots, N_{rec} \tag{B-3}$$

$$|\underset{\sim}{\mathbf{A}}_k^H(:,r)\underset{\sim}{\mathbf{A}}_l(:,q)| = \begin{cases} |\mathbf{a}_k^H \mathbf{a}_l|, & \text{if } r = q \text{ and } k \neq l \\ 0, & \text{if } r \neq q, \forall k, l \end{cases} \tag{B-4}$$

Consequently:

$$\begin{aligned} \mu_{\mathbf{A}_{ech}} = \max_{k \neq l, r=q} \left(\frac{|\underset{\sim}{\mathbf{A}}_k^H(:,r)\underset{\sim}{\mathbf{A}}_l(:,q)|}{\|\underset{\sim}{\mathbf{A}}_k(:,r)\|.\|\underset{\sim}{\mathbf{A}}_l(:,q)\|} \right) = \\ \max_{k \neq l} \left(\frac{|\mathbf{a}_k^H \mathbf{a}_l|}{\|\mathbf{a}_k\|.\|\mathbf{a}_l\|} \right) = \mu_{\mathbf{A}} \end{aligned} \tag{B-5}$$

APPENDIX C

The transformation process from the echo signal to the sparse signal model using the Xampling technique is detailed in this appendix. The Xampling scheme is known as the Multi-Channel Modulating Waveforms (MCMW) scheme and is shown in Fig. C.1.

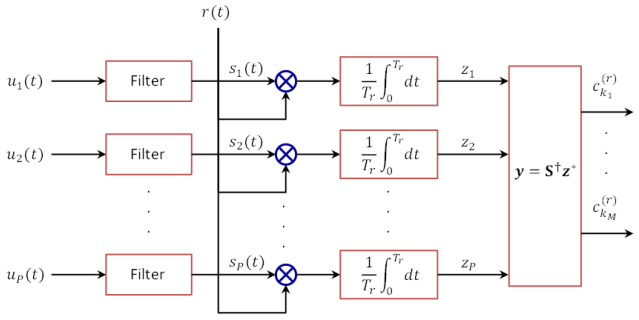

Fig. C.1: MCMW scheme for acquisition

This is a low-cost, stable, sub-Nyquist analog-to-digital conversion method that provides a limited set of the signal's Fourier Coefficients (FC) $\mathbf{y} = \{c_{k_m}^{(r)}\}_{k_m \in \mathbf{k}_M}$, whose frequency positions are identified by the subset $\mathbf{k}_M = \{k_i\}_{i=1,\dots,M}$. The T_r-periodical binary pseudorandom waveforms $\{u_i(t)\}_{i=1,\dots,P}$ are first filtered to obtain the signals $\{s_i(t) = \sum_{k=k_1}^{k_M} s_{ik} e^{j2\pi(k/T_r)t}\}_{i=1,\dots,P}$, where $\{s_{ik}\}_{\substack{i=1,\dots,P \\ k \in \mathbf{k}_M}}$ denote the Fourier coefficients of these signals within the filter bandwidth. The echo signal $r(t)$ is then mixed with the filtered waveforms $s_i(t)$, integrated during T_r and sampled at the PRF rate. The $\mathbf{z}$ vector below is thus obtained:

$$z_i = \frac{1}{T_r} \int_0^{T_r} r(t) \sum_{k=k_1}^{k_M} s_{ik} e^{j2\pi(k/T_r)t} \, dt \quad \text{for} \quad i = 1, \dots, P \tag{C-1}$$

It can be readily seen that:

$$z_i^* = \sum_{k=k_1}^{k_M} s_{i_k}^* \frac{1}{T_r} \int_0^{T_r} r(t) e^{-j2\pi(k/T_r)t} \, dt = \sum_{k=k_1}^{k_M} s_{i_k}^* c_k^{(r)} \tag{C-2}$$

So that $\mathbf{z}^* = \mathbf{S}\mathbf{y}$, where $\mathbf{S}$ is the $P \times M$ matrix $\{s_{i_k}^*\}_{\substack{i=1,\dots,P \\ k \in \mathbf{k}_M}}$. Finally, the Xampling scheme output is given by:

$$\mathbf{y} = \mathbf{S}^\dagger \mathbf{z}^* \tag{C-3}$$

where $\mathbf{S}^\dagger$ is the pseudo-inverse of the $P \times M$ matrix $\mathbf{S} = \{s_{i_k}^*\}_{\substack{i=1,\dots,P \\ k \in \mathbf{k}_M}}$.

Let us now consider the received signal model (equation (1) in the paper) and denote by $c_k^{(r)} = \frac{1}{T_r} R_q\left(\frac{k}{T_r}\right)$ and $c_k^{(p)} = \frac{1}{T_r} P\left(\frac{k}{T_r}\right)$ the FC of the periodized signals $r_q(t)$ and $p(t)$ respectively. Then, (1) can be further developed as follows:

$$r_q(t) = \sum_{l=1}^{L} \sigma_l^{(q)} p(t - \tau_l^{(q)} - qT_r) e^{-j2\pi f_l^{(q)} qT_r} \tag{C-4}$$

which leads to:

$$R_q(\nu) = \sum_{l=1}^{L} \sigma_l^{(q)} P(\nu) e^{-j2\pi(\tau_l^{(q)} + qT_r)\nu} e^{-j2\pi f_l^{(q)} qT_r} \tag{C-5}$$

Further simplifying yields:

$$R_q(\nu) = P(\nu) e^{-j2\pi qT_r \nu} \sum_{l=1}^{L} \sigma_l^{(q)} e^{-j2\pi\tau_l^{(q)}\nu} e^{-j2\pi f_l^{(q)} qT_r} \tag{C-6}$$

thus, we have:

$$c_k^{(r)} = c_k^{(p)} \sum_{l=1}^{L} \sigma_l^{(q)} e^{-j2\pi\tau_l^{(q)} \frac{k}{T_r}} e^{-j2\pi f_l^{(q)} qT_r} \tag{C-7}$$

which simplifies to:

$$c_k^{(r)} = c_k^{(p)} \sum_{l=1}^{L} x_{i_l} e^{-j2\pi i_l k/(T_r F_{Nyq})} \tag{C-8}$$

and further to:

$$c_k^{(r)} = c_k^{(p)} \sum_{l=1}^{L} x_{i_l} e^{-j2\pi i_l k/N_{DFT}} \tag{C-9}$$

When only the indices $k \in \mathbf{k}_M$ are considered, this equation can be expressed in the following matrix form:

$$y = \mathbf{\Phi}\mathbf{\Psi}\mathbf{x} = \mathbf{A}\mathbf{x} \tag{C-10}$$

where $\mathbf{\Phi}$ is the diagonal $M \times M$ matrix $\{c_{k_m}^{(p)}\}_{k_m \in \mathbf{k}_M}$ and $\mathbf{\Psi}$ is the $M \times N_{DFT}$ reduced DFT matrix $\{e^{-j2\pi k_m n/N_{DFT}}\}_{\substack{k_m \in \mathbf{k}_M \\ n=0,\dots,N_{DFT}-1}}$. This equation reveals the link between the output of the considered Xampling scheme, represented by the vector $\mathbf{y}$, and the sparse signal model $\mathbf{x}$, subject to the proposed sparse detection algorithms.